Design and Implementation of a GSI-Based Convection-Allowing Ensemble-Based Data Assimilation and Forecast System for the PECAN Field Experiment. Part II: Overview and Evaluation of a Real-Time System

AARON JOHNSON

Cooperative Institute for Mesoscale Meteorological Studies, and School of Meteorology, University of Oklahoma, Norman, Oklahoma

XUGUANG WANG AND SAMUEL DEGELIA

School of Meteorology, University of Oklahoma, Norman, Oklahoma

(Manuscript received 21 November 2016, in final form 13 March 2017)

ABSTRACT

Multiscale ensemble-based data assimilation and forecasts were performed in real time during the Plains Elevated Convection At Night (PECAN) field experiment. A 20-member ensemble of forecasts at 4-km grid spacing was initialized daily at both 1300 and 1900 UTC, together with a deterministic forecast at 1-km grid spacing initialized at 1300 UTC. The configuration of the GSI-based data assimilation and forecast system was guided by results presented in Part I of this two-part study. The present paper describes the implementation of the real-time system and the extensive forecast products that were generated to support the unique interests of PECAN researchers. Subjective and objective verification of the real-time forecasts from 1 June through 15 July 2015 is conducted, with an emphasis on nocturnal mesoscale convective systems (MCSs), nocturnal convective initiation (CI), nocturnal low-level jets (LLJs), and bores on the nocturnal stable layer. Verification of nocturnal precipitation during overnight hours, a proxy for MCSs, shows both greater skill and spread for the 1300 UTC forecasts than the 1900 UTC forecasts. Verification against observed soundings reveals that the forecast LLJs systematically peak, veer, and dissipate several hours before the observations. Comparisons with bores that passed over an Atmospheric Emitted Radiance Interferometer reveal an ability to predict borelike features that is greatly improved at 1-km, compared with 4-km, grid spacing. Objective verification of forecast CI timing reveals strong sensitivity to the PBL scheme but an overall unbiased ensemble.

1. Introduction

One of the goals of the Plains Elevated Convection At Night (PECAN; Geerts et al. 2017) experiment is to improve predictions of nocturnal convection and related features, including mesoscale convective systems (MCSs), convective initiation (CI), bores, and low-level jets (LLJs) "*with a particular focus on the next generation convective-permitting models and advanced assimilation techniques*" (Parsons et al. 2013). Comprehensive observations in the PECAN Integrated Sounding Array (PISA) were made of such nocturnal convection features during PECAN. In addition to mobile platforms, six fixed PISA (FP) sites were strategically placed across the PECAN domain to collect regular observations at predictable locations throughout the field experiment (Parsons et al. 2013). These observations compose a unique and valuable dataset for data assimilation (DA) and model validation studies. Johnson and Wang (2017), which is Part I of this paper, described a series of experiments designed to better understand optimal convection-permitting ensemble forecasts and storm-scale DA configurations for the prediction of nocturnal convection and related features using retrospective forecasts from 2014. The GSI-based multiscale ensemble DA and forecast system described in Part I and Johnson et al. (2015) was also implemented as an operational real-time nocturnal-convection prediction system during the PECAN field experiment. This system is described and evaluated in the present paper.

The ensemble Kalman filter (EnKF) has been a popular choice in research studies involving storm-scale or multiscale convection-permitting ensemble simulations with radar DA (e.g., Snyder and Zhang 2003;

Corresponding author: Dr. Aaron Johnson, ajohns14@ou.edu

DOI: 10.1175/WAF-D-16-0201.1

Zhang et al. 2004; Dowell et al. 2004; Aksoy et al. 2010; Yussouf and Stensrud 2010; Jung et al. 2012; Wheatley et al. 2014,2015; Johnson et al. 2015; Wang and Wang 2017). The EnKF has also been applied at mesoscale or coarser resolutions to obtain initial conditions (ICs) for convection-permitting ensemble forecasts (Jones and Stensrud 2012; Melhauser and Zhang 2012; Schumacher and Clark 2014; Romine et al. 2014; Schwartz and Liu 2014; Schwartz et al. 2014, 2015a,b). Given the computational cost of ensemble-based DA, the use of EnKF in real-time convection-permitting ensembles has been much more limited in published studies (e.g., Schwartz et al. 2015b; Wheatley et al. 2015). For example, Schwartz et al. (2015b) make the computational cost tractable by doing the DA on a coarser mesoscale grid without radar observations. Wheatley et al. (2015) focus on Warn-on-Forecast time and space scales and limit the forecast lead times to about 1 h. Both of these studies focus on severe weather prediction, which occurs primarily during the day. The prediction system described in this paper is unique in its focus on nocturnal convection. Furthermore, multiscale cycled EnKF is conducted using radar observations on the convection-permitting grid, and assimilating conventional surface and upper-air observations to provide the mesoscale environment for the radar DA, while also generating ensemble forecasts out to the 2-day lead time.

Another unique aspect of the prediction system described in this paper is that it represents the first time, to the authors' knowledge, that the GSI-based framework has been used for real-time convective-scale DA and forecasting. Since the system is GSI based, it uses the operational (nonradar) observation data stream and quality control from the National Centers for Environmental Prediction (NCEP). This work therefore helps facilitate the move toward meso/convective-scale ensemble-based DA and forecasting at NCEP.

In addition to a 20-member ensemble of forecasts with 4-km grid spacing, a 24-h deterministic forecast with 1-km grid spacing over the central United States was also generated daily during PECAN. Previous research has shown advantages of 1-km, relative to 4-km, grid spacing only for scales that are not resolved at the 4-km grid spacing (e.g., Johnson et al. 2013). Bryan et al. (2003) have shown that grid spacing on the order of 100 m may be needed to fully resolve moist convective systems, as a result of the sensitivity to small-scale boundary layer and turbulence processes. However, a major focus of PECAN is to better understand and improve the predictability of atmospheric bores and their interaction with nocturnal convection (Haase and Smith 1989; Parsons et al. 2013). A 1-km deterministic forecast was included in the real-time forecasts to test the hypothesis that such resolution is necessary, and perhaps adequate, to better resolve and more accurately predict bores and other wavelike features on the nocturnal stable layer.

Atmospheric bores can occur when a density current impinges on a low-level temperature inversion that acts as a ducting layer for wave energy (Rottman and Simpson 1989; Lutzak 2013). A bore is characterized by a steplike increase in the height of the inversion and a corresponding semipermanent increase in surface pressure in advance of the density current. The "undular" type of bore may also be associated with oscillations in the surface pressure and inversion height (Rottman and Simpson 1989; Lutzak 2013). Bores are frequently generated in the Great Plains when cold thunderstorm outflows interact with the nocturnal stable layer (e.g., Haghi and Parsons 2014). Bores can also play an important role in the generation and maintenance of subsequent nocturnal convection (e.g., Karyampudi et al. 1995). Understanding and improving the predictability of atmospheric bores on the nocturnal stable layer is therefore one of the primary goals of PECAN (Parsons et al. 2013). The unique field observations during PECAN, such as temperature and moisture retrievals by the Atmospheric Emitted Radiance Interferometer (AERI; Turner and Löhnert 2014) at the FP sites, together with the forecast system described in the present paper, facilitate this goal of PECAN.

In addition to bores, the PECAN objectives are focused on nocturnal MCSs, nocturnal CI, and the nocturnal LLJ (Parsons et al. 2013). Nocturnal MCSs can result from the upscale growth of afternoon convection as well as the initiation of new convection during the overnight hours. Idealized modeling studies (e.g., Parker 2008; French and Parker 2010) and observation-based case studies (e.g., Weckwerth et al. 2004) have shown the importance of other nocturnal features such as bores and LLJs in the maintenance and evolution of nocturnal MCSs. Ensemble simulations of many MCSs over an extended time period, such as the real-time PECAN forecasts described in the present paper, provide an opportunity to further understand the processes governing their organization and maintenance. Such understanding is needed to improve the predictability of nocturnal MCSs in convection-permitting forecasts. Unlike daytime CI, which is often associated with convergence along surface boundaries (e.g., Weckwerth and Parsons 2006; Parsons et al. 2013), nocturnal CI tends to be elevated and has received much less attention in the scientific literature (e.g., Wilson and Roberts 2006). Furthermore, the evaluation of model CI forecasts is complicated by difficulties such as distinguishing newly initiated convection from ongoing convection (Kain et al. 2013). The nocturnal LLJ has long been known to

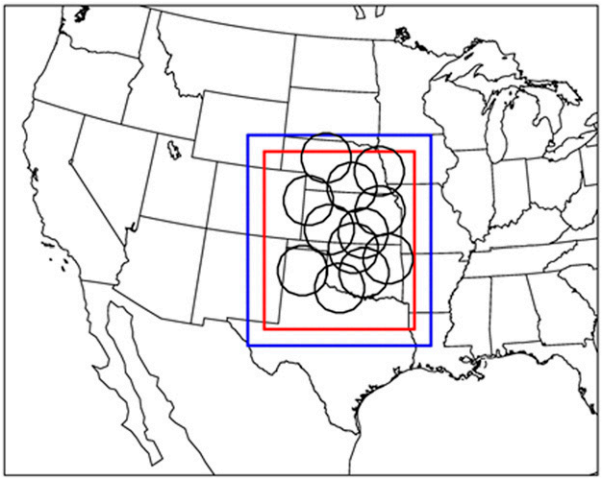

FIG. 1. Model domains used in this study. The outermost domain has a grid spacing of 12 km. The domain enclosed by the blue box has a grid spacing of 4 km, and the domain enclosed by the red box has a grid spacing of 1 km. Black circles indicate the coverage areas of each radar site used for data assimilation.

play a role in both the initiation and maintenance of nocturnal convection (e.g., Bonner 1966; French and Parker 2010; Marsham et al. 2011). The model predictability of the nocturnal LLJ is therefore also an important component of nocturnal convection to consider.

The purpose of this paper is to document the details of the real-time GSI-based multiscale ensemble DA and forecast system that was implemented during PECAN and to evaluate the performance of the system within the context of the above PECAN foci. The system configuration and forecast products are described in section 2 and evaluation of the system is presented in section 3. Section 4 contains a summary and conclusions.

2. System configuration and forecast products

a. Configuration

The configuration of the ensemble DA and forecast system for the PECAN real-time forecasts is summarized in Figs. 1 and 2 and Tables 1 and 2. The DA component of the system is a 40-member GSI-based EnKF (Johnson et al. 2015). The outermost domain has 12-km grid spacing and covers approximately the conterminous United States (Fig. 1). Following Johnson et al. (2015), observations from the NCEP regional DA system (e.g., conventional surface and upper-air observations), which included many special fixed-site soundings from the PECAN field experiment, are assimilated on the 12-km grid every 3 h starting at 0000 UTC. At 1200 UTC, and again at 1800 UTC, the 12-km analyses and short-term forecasts are downscaled to a domain covering the central United States with 4-km grid spacing (blue box in Fig. 1). Radar reflectivity and radial velocity observations are then assimilated on the 4-km grid every 15 min for a period of 1 h. The 15-min cycling

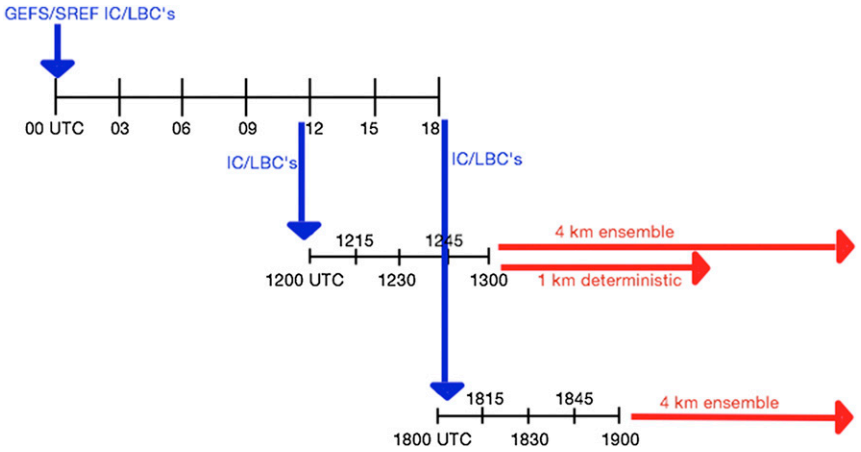

FIG. 2. Schematic of daily data assimilation cycling configuration. Ensemble analyses and forecasts from the 0000 and 2100 UTC cycles, respectively, of the NCEP GEFS and SREF provide ICs and LBCs for assimilation of nonradar observations on an outer 12-km domain every 3 h from 0000 to 1800 UTC (top timeline). At 1200 UTC, the analyses and short-term forecasts from the outer domain assimilation are downscaled to the 4-km domain and radar observations are assimilated every 15 min for 1 h (center timeline; not to scale with top timeline). The analyses at 1300 UTC provide ICs for the 4-km ensemble and 1-km deterministic forecasts (red arrows). Note that 10 of the 4-km ensemble members are 2-day forecasts while the other 10 members are 1-day forecasts. The process is repeated at 1800 UTC, except without an update of the 1-km forecast (bottom timeline).

TABLE 1. Summary of forecasts generated daily in support of PECAN field operations.

Initialization time (UTC)	No. of members	Grid spacing (km)	No. of vertical levels	Forecast range (h)
1300	20	4	50	24
1300	10	4	50	48
1300	1	1	50	24
1900	20	4	50	18
1900	10	4	50	42

was chosen because of time and resource constraints, although Part I found slight forecast advantages to cycling the radar DA every 10 min. Forecasts were initialized from the resulting analyses at 1300 and 1900 UTC daily from 1 June through 15 July 2015 (Table 1). The 1300 and 1900 UTC initialization times were chosen to balance the need for a recently initialized forecast with the need to have the forecast products delivered in time for the PECAN forecasters to use while preparing the daily 2000 and 0200 UTC forecast briefings, respectively.

At 1300 UTC, a 20-member ensemble forecast was initialized on the 12- and 4-km grids. The first 10 members were run to the 48-h lead time and the second 10 members were run to the 24-h lead time (Fig. 2 and Table 1). Thus, a 20-member ensemble was available to PECAN forecasters for the night 1 forecast as well as a 10-member ensemble for the night 2 forecast. A deterministic forecast at 1-km resolution (red box in Fig. 1) was also initialized at 1300 UTC from the ensemble mean of the 4-km analyses and run to the 24-h lead time. Additional 12- and 4-km ensemble forecasts were then initialized from the 1900 UTC analyses and were available for the evening update of both the night 1 and night 2 forecasts. The 1-km deterministic forecast was not initialized at 1900 UTC because of time and computer resource constraints. Examples of the forecast products made available to the forecasters are shown in the following subsection.

The sources of ensemble diversity are summarized in Table 2. Each ensemble member was initialized with, and obtained lateral boundary conditions (LBCs) from, either a Global Ensemble Forecast System (GEFS; Toth et al. 2004; Wei et al. 2008) or a Short-Range Ensemble Forecast (SREF; Du et al. 2014) member from the cycle initialized at 0000 UTC of the assimilation day or 2100 UTC of the previous day, respectively. On the outer (12 km) grid, three different cumulus parameterization schemes were used (Table 2). The microphysics scheme during DA was the WRF single-moment 6-class (WSM6; Hong and Lim 2006) with parameter perturbations (Part I). During the 2014 forecasts described in Part I, the comparison between the Thompson and WSM6 schemes was mixed, with the Thompson scheme showing poorer performance than WSM6 at earlier lead times and better performance for the night 1 forecasts (Figs. 2g,h,i in Part I). As a result of the greater computational cost of Thompson, which was important under the forecast time constraints, WSM6 was chosen in the 2015 real-time experiments. A fixed quasi-normal scale elimination (QNSE; Sukoriansky et al. 2005) boundary layer parameterization was used during DA (Table 2) since this configuration provided the best overall performance during the 2014 forecasts, as described in Part I. The forecast ensemble microphysics and boundary layer parameterization configurations in Table 2 follow the "MULTI" configuration from Part I because this configuration provided the best combination of forecast performance and ensemble spread of the three configurations considered in Part I (see also Johnson et al. 2011). All ensemble members used the Noah land surface model, Goddard shortwave radiation, and RRTMG longwave radiation schemes.

b. *Forecast products and examples*

The forecast products generated from the ensemble forecast system were tailored to the unique interests of the PECAN forecasters and researchers by emphasizing nonstandard fields that were expected to be useful for the prediction of nocturnal MCSs, nocturnal CI, bores, and LLJs. A detailed summary of these forecast products is provided in the appendix. In this section, examples of MCS, CI, and bore event forecasts are demonstrated, and some of the subjectively identified successes and limitations of the forecasts are described. The examples shown in this section are selected because they are representative of both the systematic successes and limitations of the forecast system that were noted during PECAN.

The ensemble forecast initialized at 1300 UTC 3 June shows a broad area of scattered storms at 0600 UTC 4 June (Fig. 3a), which approximately covers the area in northeast Kansas and southeast Nebraska where such storms are also observed (Fig. 3c). The ensemble forecast also shows storms developing in the high plains of northeast Colorado, as observed, although it does not predict the storms farther south in eastern Colorado, which leads to a bowing line segment in northwestern Kansas in the observations (Fig. 3d). Several other deterministic convection-allowing forecasts available to the PECAN forecasters incorrectly indicated a single large MCS moving southeast through northeastern Kansas by 0900 UTC (not shown). In contrast, the ensemble successfully predicts the presence of multiple smaller MCSs as well as high uncertainty about storm location, although the mean

TABLE 2. Physics and IC configuration of the different ensemble members, including configurations during the DA and forecast periods and including PBL, microphysics (MP), and cumulus (CP) parameterizations. See text for descriptions of the WSM6 parameter perturbations; N/A indicates not applicable (e.g., forecasts were not generated for members 021–040).

Name	DA PBL	Forecast PBL	DA MP	Forecast MP	12-km CP	IC/LBC
Hi-res	N/A	MYNN	N/A	Thompson	Grell-3	4-km mean/ member 001 forecast
001	QNSE	MYNN	WSM6	Thompson	Grell-3	GEFS.001
002	QNSE	QNSE	WSM6	WDM6	Kain–Fritsch	GEFS.002
003	QNSE	YSU	WSM6	Lin	Kain–Fritsch	GEFS.003
004	QNSE	ACM2	WSM6	Thompson	Grell-F	GEFS.004
005	QNSE	MYJ	WSM6	WDM6	Grell-3	GEFS.005
006	QNSE	MYNN	WSM6	Morrison	Kain–Fritsch	GEFS.006
007	QNSE	QNSE	WSM6	Thompson	Kain–Fritsch	GEFS.007
008	QNSE	YSU	WSM6	WDM6	Grell-F	GEFS.008
009	QNSE	ACM2	WSM6	Lin	Grell-3	GEFS.009
010	QNSE	MYJ	WSM6	Thompson	Kain–Fritsch	GEFS.010
011	QNSE	MYNN	WSM6	WDM6	Kain–Fritsch	GEFS.011
012	QNSE	QNSE	WSM6	Morrison	Grell-F	GEFS.012
013	QNSE	YSU	WSM6	Thompson	Grell-3	GEFS.013
014	QNSE	ACM2	WSM6	WDM6	Kain–Fritsch	GEFS.014
015	QNSE	MYJ	WSM6	Thompson	Kain–Fritsch	GEFS.015
016	QNSE	MYNN	WSM6	Morrison	Grell-F	GEFS.016
017	QNSE	QNSE	WSM6	Thompson	Grell-3	GEFS.017
018	QNSE	YSU	WSM6	Thompson	Kain–Fritsch	GEFS.018
019	QNSE	ACM2	WSM6	Thompson	Kain–Fritsch	GEFS.019
020	QNSE	MYJ	WSM6	Thompson	Grell-F	GEFS.020
021	QNSE	N/A	WSM6	N/A	Grell-3	SREF_em.ctl
022	QNSE	N/A	WSM6	N/A	Kain–Fritsch	SREF_em.n1
023	QNSE	N/A	WSM6	N/A	Kain–Fritsch	SREF_em.p1
024	QNSE	N/A	WSM6	N/A	Grell-F	SREF_em.n2
025	QNSE	N/A	WSM6	N/A	Grell-3	SREF_em.p2
026	QNSE	N/A	WSM6	N/A	Kain–Fritsch	SREF_em.n3
027	QNSE	N/A	WSM6	N/A	Kain–Fritsch	SREF_em.p3
028	QNSE	N/A	WSM6	N/A	Grell-F	SREF_nmm.ctl
029	QNSE	N/A	WSM6	N/A	Grell-3	SREF_nmm.n1
030	QNSE	N/A	WSM6	N/A	Kain–Fritsch	SREF_nmm.p1
031	QNSE	N/A	WSM6	N/A	Kain–Fritsch	SREF_nmm.n2
032	QNSE	N/A	WSM6	N/A	Grell-F	SREF_nmm.p2
033	QNSE	N/A	WSM6	N/A	Grell-3	SREF_nmm.n3
034	QNSE	N/A	WSM6	N/A	Kain–Fritsch	SREF_nmm.p3
035	QNSE	N/A	WSM6	N/A	Kain–Fritsch	SREF_nmb.n1
036	QNSE	N/A	WSM6	N/A	Grell-F	SREF_nmb.p1
037	QNSE	N/A	WSM6	N/A	Grell-3	SREF_nmb.n2
038	QNSE	N/A	WSM6	N/A	Kain–Fritsch	SREF_nmb.p2
039	QNSE	N/A	WSM6	N/A	Kain–Fritsch	SREF_nmb.n3
040	QNSE	N/A	WSM6[a]	N/A	Grell-F	SREF_nmb.p3

location is displaced slightly south of where the storms are observed (Figs. 3b,d). This case illustrates the importance of convection-permitting ensemble forecasts for the nocturnal evolution of MCSs with relatively low predictability (i.e., high uncertainty).

Prediction of elevated nocturnal CI is another particularly challenging problem for forecasters. At 0400 UTC 24 June, both the forecast (initialized at 1300 UTC 23 June) and observations show no convection in far eastern Nebraska and southern Iowa (Figs. 4a,c). Just 2 h later elevated convection has initiated in both southwestern Iowa and eastern Nebraska in the observations (Fig. 4d). The ensemble forecast successfully identifies the occurrence of this CI as well as the orientation of northwest-to-southeast bands of cells, although with a mean location error (Fig. 4b). In this case, the observations first show convection in Iowa at ~0500 UTC. About half of the ensemble members predicted this CI to occur between 0400 and 0500 UTC and half predicted CI between 0500 and 0600 UTC, indicating an unbiased timing forecast for CI on this case (not shown). The ensemble successfully predicts similar elevated nocturnal convection in several other cases as well, although the observed CI location did

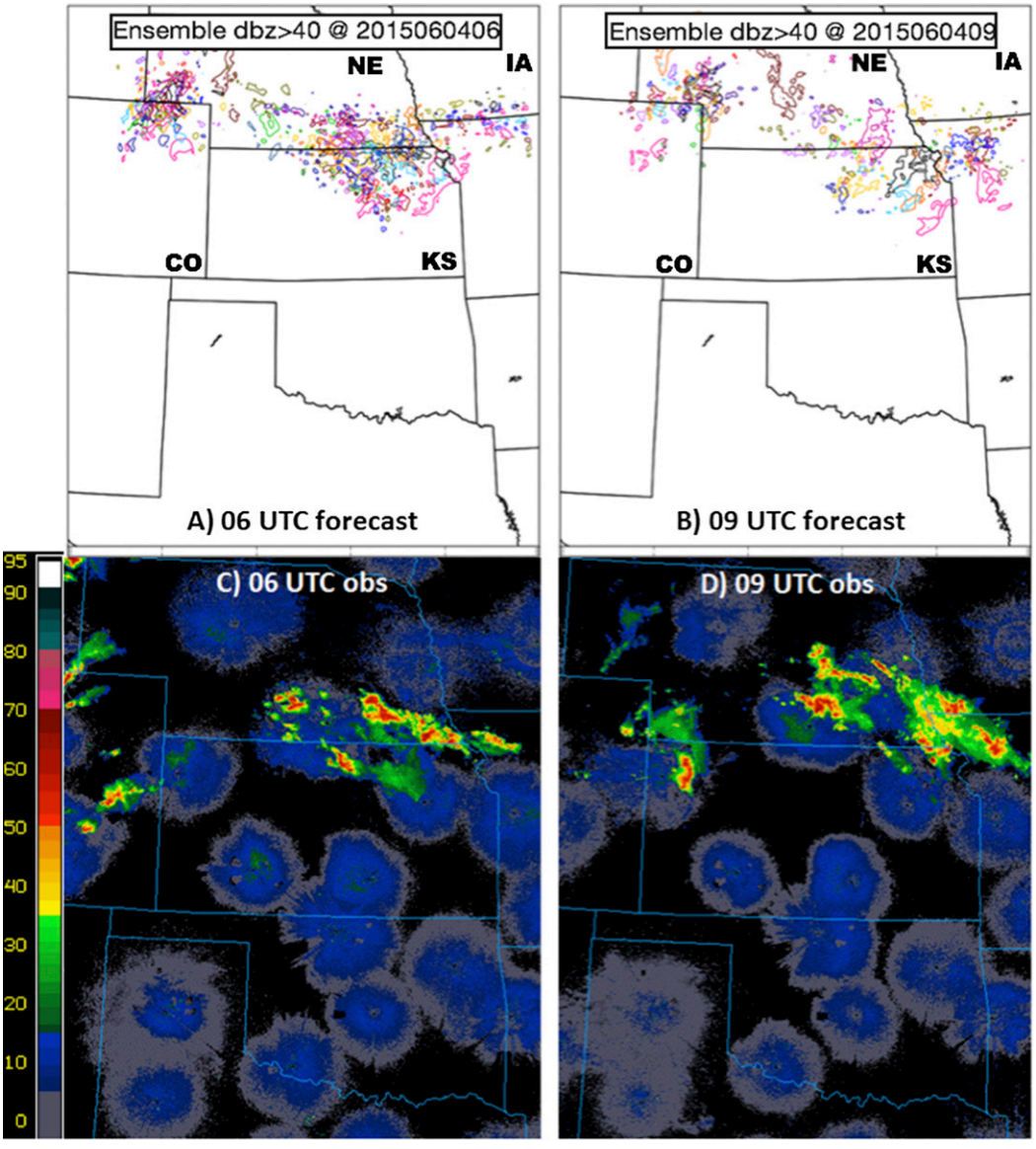

FIG. 3. Ensemble spaghetti plot of the 40-dBZ contour of 1 km AGL reflectivity for the forecast initialized at 1300 UTC 3 Jun 2015 and valid at (a) 0600 and (b) 0900 UTC 4 June 2015, as well as observed composite reflectivity mosaic at (c) 0600 and (d) 0900 UTC 4 Jun 2015.

fall outside of the envelope of ensemble members on several cases (not shown). Other studies are ongoing, focused specifically on the problem of predicting nocturnal CI (e.g., Degelia et al. 2016, unpublished manuscript), and a preliminary CI objective verification is presented in section 3. The subjectively large location errors of the entire ensemble in both of the above CI and MCS events were noted systematically throughout the PECAN experiment and are a subject of future research.

During the PECAN field experiment, the 1-km deterministic forecast repeatedly demonstrated an ability to explicitly predict borelike features corresponding to observed bores. For example, at ~0700 UTC 5 June 2015 a bore was observed in southwest Kansas that is evident as parallel fine lines ahead of a decaying MCS in the Dodge City, Kansas (KDDC), observed reflectivity (Fig. 5a). The 1-km above ground level vertical velocity from the 1-km deterministic forecast shows a similar feature in southwest Kansas (Fig. 5b). Examination of the corresponding surface temperature forecast (Fig. 5c) reveals that this wave train is associated with a bore, rather than a cold pool, since the leading edge of the wave train is collocated with a slight increase, rather

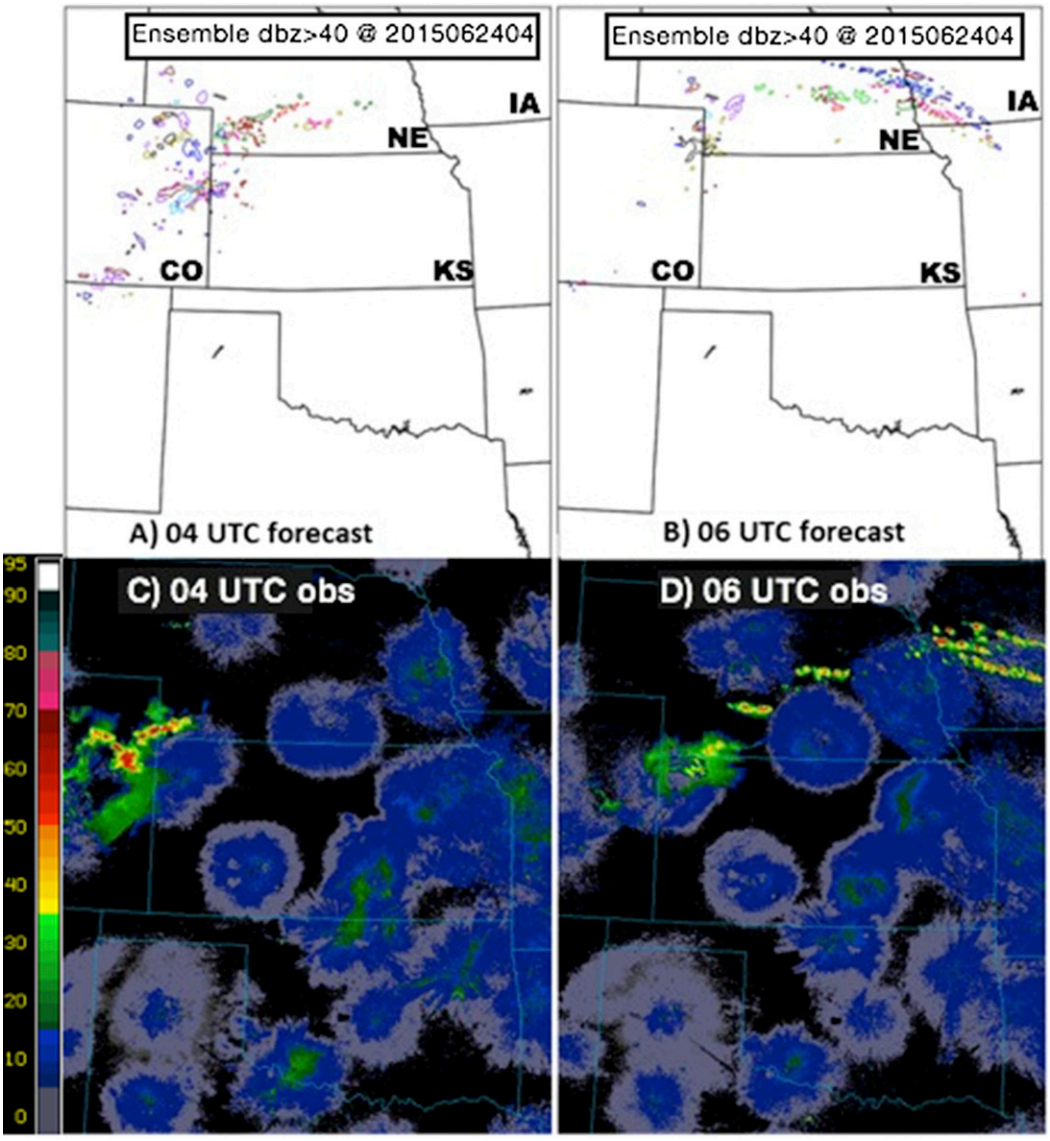

FIG. 4. As in Fig. 3, but for forecasts initialized at 1300 UTC 23 Jun 2015 and valid times of (a),(c) 0400 and (b),(d) 0600 UTC 24 Jun 2015.

than decrease, in the surface temperature. Note that the wind shift and corresponding convergence at the bore passage is also consistent with observed bores (Fig. 5c). The 1-km forecast was successfully able to resolve similar borelike features, although the predictability of specific bores was limited largely by the predictability of antecedent convection leading to density currents. The realism of the simulated bores is further evaluated in section 3.

The above paragraphs demonstrate the ability of the ensemble-based DA and forecast system to contribute to better understanding and improving the predictability of nocturnal convective features. However, the forecasts were still limited in their ability to *consistently* improve upon deterministic and convection-parameterizing operational forecasts of nocturnal MCSs in all cases, their ability to pinpoint the locations of elevated nocturnal CI with less than several hundred kilometers of uncertainty, and their ability to predict the times and locations of density currents leading to atmospheric bores. Similar cases, as well as LLJ cases, are further evaluated in the following section, which also provides more systematic and quantitative verification measures that can serve as benchmarks for further improvements to the practical predictability of nocturnal convection in future studies.

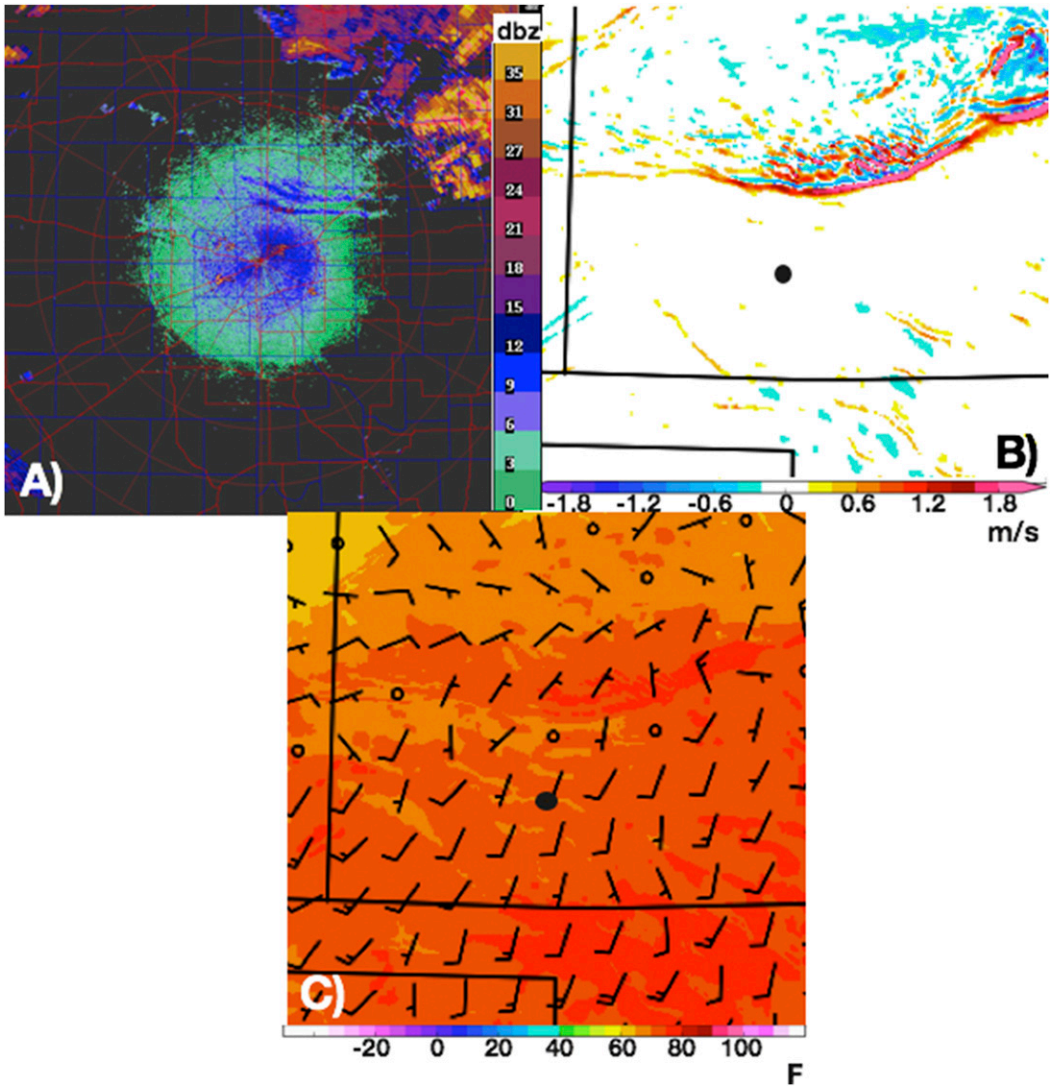

FIG. 5. (a) Observed reflectivity from KDDC at 0652 UTC 5 Jun, (b) 1 km AGL vertical velocity forecast from 1-km member initialized at 1300 UTC 4 Jun and valid at 0700 UTC 5 Jun, and (c) the corresponding 2-m temperature forecast from the 1-km member. All three panels cover the same domain, and the radar location in (a) is shown as a black dot in (b) and (c).

3. Forecast verification

The following forecast verification follows the verifications in Part I in that it is separated into different components, focused on the unique foci of PECAN. Verification methods appropriate for evaluating the predictability of nocturnal MCSs, nocturnal LLJs, atmospheric bores, and nocturnal CI forecasts are employed in each of the four subsections, respectively. The period of PECAN field operations covering 1 June–15 July 2015 was particularly active in terms of nocturnal convection (Geerts et al. 2017, their Fig. 1). Officially, there were 14, 6, and 11 intensive observing periods where the focus was MCS, bore, and CI/LLJ objectives, respectively, although similar features were also unofficially observed on most off nights (Geerts et al. 2017). Therefore, many robust results are obtained from the 45-day period of forecasts.

a. *Precipitation verification as proxy for MCS prediction*

As in Part I, the ensemble precipitation forecasts during overnight hours (i.e., approximately 0300–0900 UTC) are used as a proxy for verifying the nocturnal MCS forecasts. In Figs. 6a–c the Brier skill score (BSS) of the ensemble forecasts initialized at both 1300 and 1900 UTC is calculated as in Part I, with the National Severe Storms Laboratory (NSSL) Next Generation Multisensor QPE (Q2)

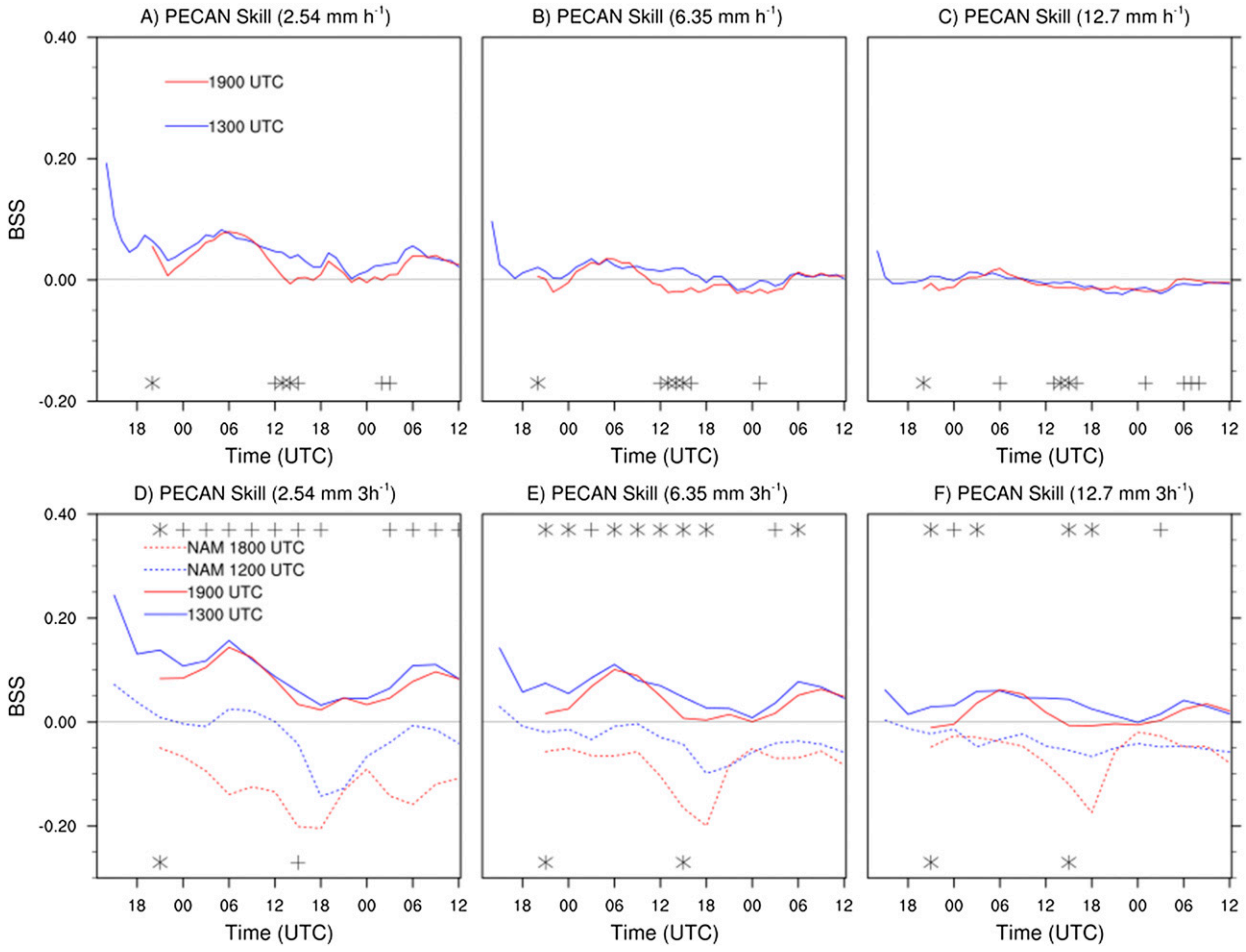

FIG. 6. BSSs for hourly thresholds of (a) 2.54, (b) 6.35, and (c) 12.7 mm h^{-1} for the real-time PECAN forecasts and for 3-hourly thresholds of (d) 2.54, (e) 6.35, and (f) 12.7 mm (3 h)$^{-1}$ for both real-time PECAN forecasts (solid) and operational NAM forecasts during the same period (dashed). Significant differences between the blue and red solid (dashed) lines are indicated by markers along the bottom (top) axes. Significance at the 80% (90%) level is indicated by a plus sign (asterisk).

product (Zhang et al. 2011) as the verifying observation and the domain-average observed precipitation frequency as the reference forecast. Statistical significance in Figs. 6 and 7 is calculated using permutation resampling, following Part I. The skill of the 1300 UTC ensemble forecasts is positive for both night 1 and night 2 at the 2.54 mm h^{-1} threshold (Fig. 6a), night 1 at the 6.35 mm h^{-1} threshold (Fig. 6b), and part of night 1 at the 12.7 mm h^{-1} threshold (Fig. 6c). The 1900 UTC ensemble forecast skill is generally less than or equal to the 1300 UTC skill, despite the later initialization time (Fig. 6). The skill of the operational (using 12-km grid spacing and cumulus parameterization) North American Mesoscale (NAM[1]; Janjić 2003) model 3-hourly forecast precipitation is plotted in Figs. 6d–f, along with the 3-hourly precipitation forecasts from the PECAN forecasts for comparison. Like the PECAN ensemble, the NAM forecasts initialized at 1800 UTC are actually less skillful than the longer-lead-time forecasts initialized 6 h earlier. This may be due to the lack of rawinsonde observations for assimilation in the 1800 UTC analyses. The substantially greater skill of the PECAN ensemble than the NAM forecast is likely due to both the use of an ensemble instead of a single deterministic forecast and the convection-permitting resolution of the PECAN ensemble.

As described in greater detail in Part I, the correspondence ratio (CR) is a measure of the spread of the ensemble precipitation forecasts, with smaller CR (i.e., less ensemble agreement) indicative of greater spread. Figure 7 shows that the 1300 UTC ensemble generally has greater spread than the 1900 UTC ensemble,

[1] NAM data were obtained from the National Operational Model Archive and Distribution System (NOMADS; http://nomads.ncdc.noaa.gov).

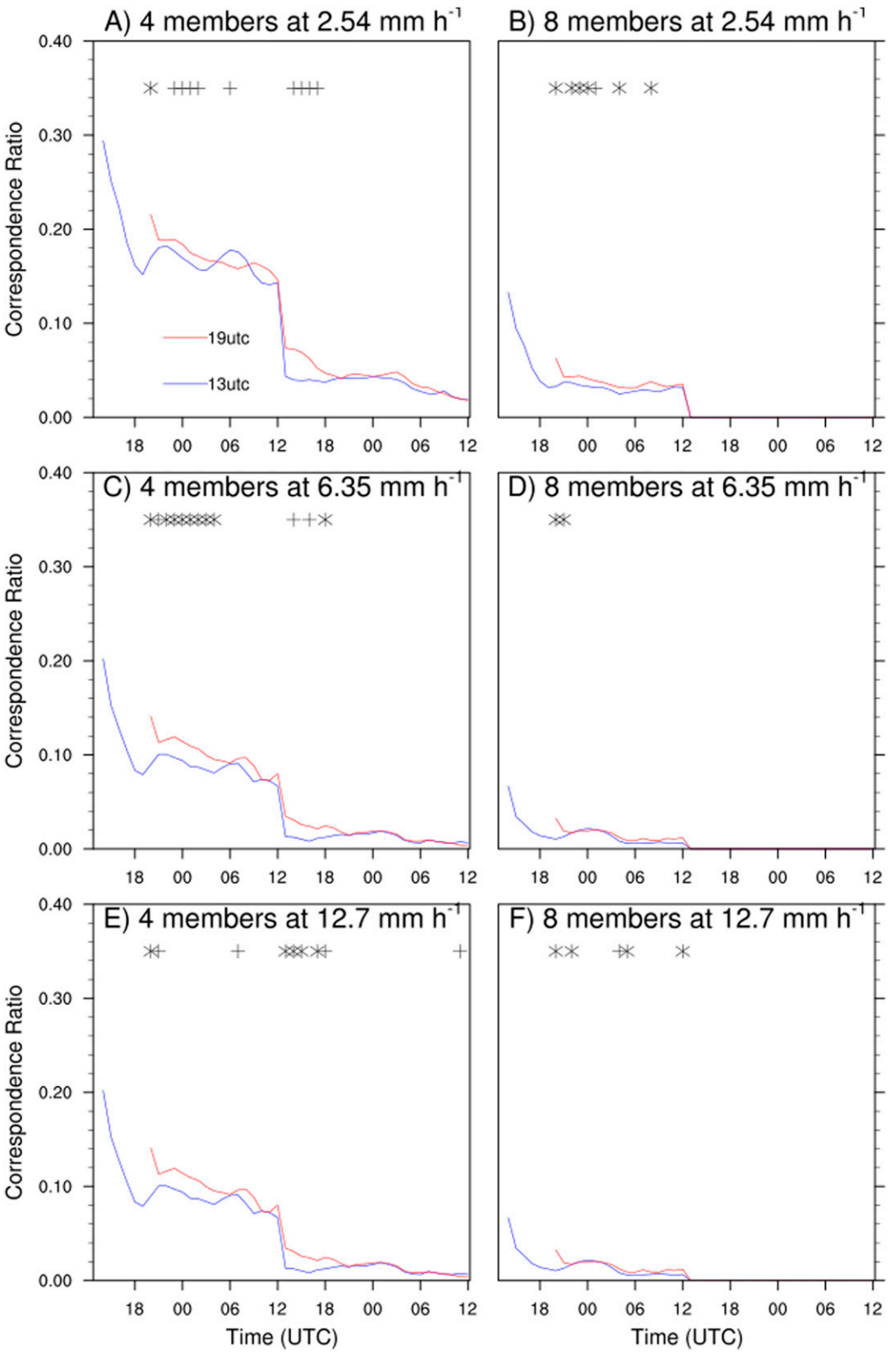

FIG. 7. Correspondence ratio for (a) 2.54 mm h^{-1} four-member agreement, (b) 2.54 mm h^{-1} eight-member agreement, (c) 6.35 mm h^{-1} four-member agreement, (d) 12.7 mm h^{-1} eight-member agreement, (e) 2.54 mm h^{-1} four-member agreement, and (f) 2.54 mm h^{-1} eight-member agreement, for the 1300 (blue) and 1900 UTC (red) initialized forecasts. Statistical significance is indicated as in Fig. 6.

in addition to the greater skill, especially at the higher forecast thresholds (e.g., Figs. 7c,e). The greater spread of the 1300 UTC ensemble (Fig. 7) is expected since the spread has more time to grow in a longer-lead-time forecast and may contribute to the greater skill of that ensemble (Fig. 6). The following results all focus on the 1300 UTC ensemble. It should be noted that the sudden drop in CR is a result of the decrease in ensemble size from 20 members to 10 members for the day 2 forecast. This causes the nominal agreement of four (eight) members to suddenly change from 20% (40%) to 40% (80%) of the ensemble. It should also be noted that the CR only reveals differences in spread, but not the quality of spread (i.e., whether it accurately reflects the mean error). The correspondence between spread and error is more easily evaluated with the nonprecipitation variables in the following subsection.

b. *Sounding verification with emphasis on LLJ prediction*

Soundings released from four of the six FP sites are used to evaluate the ensemble forecasts with greater temporal resolution than possible with the regular 12-hourly NWS soundings (Vermeesch 2015; Clark 2016; UCAR/NCAR–Earth Observing Laboratory 2016a,b). Since soundings take approximately an hour to rise through the troposphere, the verification is done by employing the GSI capability, typically used for four-dimensional DA, to compare model forecasts to observations at different times by interpolating hourly model forecast output to the time of each observation. The root-mean-square error (RMSE; solid) and ensemble spread[2] (dashed) of temperature, water vapor, and wind (components) for soundings launched at approximately 3-h intervals are shown in Fig. 8. While temperature and wind generally show good statistical consistency (i.e., similarity of spread and error), the moisture forecasts tend to be overdispersive up to about 500 hPa (Figs. 8c,d). The corresponding plots of the model bias reveal a generally warm bias at most times and heights (Figs. 9a,b), a low-level dry bias (Figs. 9c,d), and a low-level wind bias that varies with time (Figs. 9e,f). The time-varying low-level wind biases are related to systematic errors in the LLJ forecasts as explained further below.

Two representative case studies are subjectively examined to better understand the systematic biases in the predictions of the nocturnal LLJ. For both cases, the FP3 [the FP3 location can be seen in Parsons et al. (2013)] forecast and observed soundings are also generally representative of the other FP sites. The first case of forecasts initialized at 1300 UTC 9 June 2015 and valid at 0000–0900 UTC 10 June is a clean example of a nocturnal LLJ in otherwise weak ambient flow (Fig. 10). Observed soundings launched every 3 h (black lines in Fig. 10) show a very shallow LLJ maximum developing by 0600 UTC at about 500 m (Fig. 10c) and veering slightly between 0600 and 0900 UTC (Fig. 10d). In contrast to the observed LLJ, the forecasts first show the shallow LLJ 3 h earlier at 0300 UTC (Fig. 10b). The forecast LLJs also veer more strongly with time and decay in magnitude earlier than the observed LLJ (Figs. 10c,d). The early maximum and early veering in the forecasts are quantified in Table 3. Table 3 also shows that while the observed LLJ maximum descends in altitude (i.e., increasing pressure) by about 23 mb (1 mb = 1 hPa) between 0300 and 0900 UTC, the forecast LLJ maximum actually ascends in altitude by about 7 mb. These characteristics are consistent across all PBL schemes for this case (Table 3).

The second case of forecasts initialized at 1300 UTC 19 June 2015 and valid at 0000–0900 UTC 20 June is an example of an LLJ developing within stronger ambient flow, creating a larger hodograph that is more representative of hodographs likely to be encountered when forecasting for organized nocturnal convection (Fig. 11). In this case the observations show a deeper LLJ maximum of about 15 m s^{-1} between about 500 and 1000 m at 0300 UTC that further intensifies to about 25 m s^{-1} at ~500 m at 0600 UTC (Figs. 11b,c). By 0900 UTC the observed LLJ still has a maximum near 25 m s^{-1} at about 500 m but has now veered to the southwest, following the typical evolution of observed LLJs (e.g., Vanderwende et al. 2015). Like the first case, the corresponding forecast soundings show an LLJ that begins to intensify and veer much earlier than observed (Figs. 11a,b), especially for ensemble members with the QNSE PBL scheme (green lines in Fig. 11). Also like the first case, the forecast LLJ dissipates earlier than observed (Fig. 11d). For this case, the LLJ maximum descends in altitude slightly between 0300 and 0900 UTC for both forecasts and observations, and the early veering and dissipation is most pronounced for the QNSE PBL scheme (Table 4).

c. *Subjective evaluation of bores passing over fixed PISA AERI instruments*

This section provides a subjective, qualitative evaluation of an observed bore. The bore was observed by the

[2] Since RMSE necessarily contains both the variance of the model error and the observation error, the observation error variance is also added to the ensemble variance for a direct comparison to RMSE.

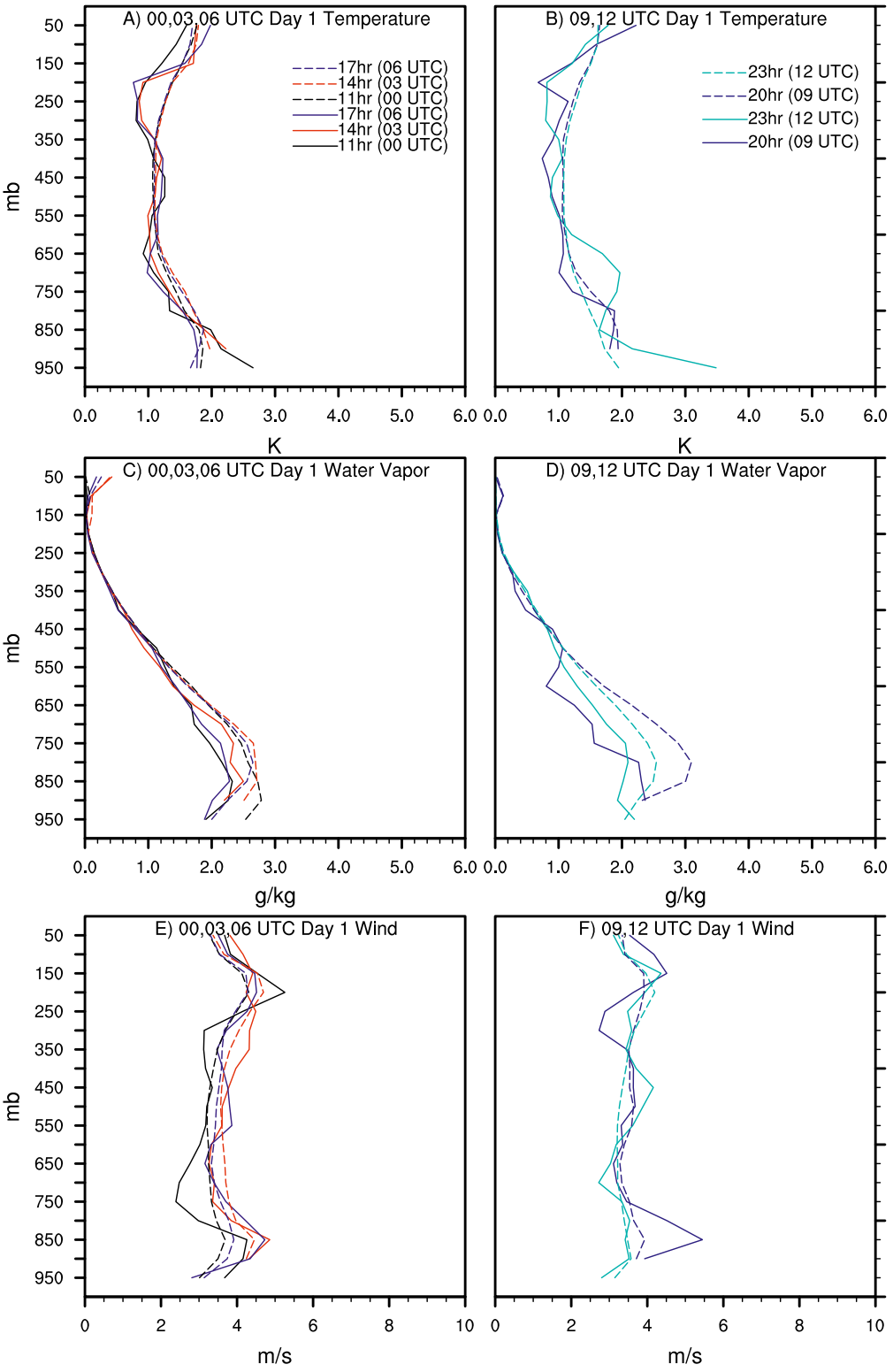

FIG. 8. RMSE (solid), from observed soundings at FP sites, of ensemble mean forecasts initialized at 1300 UTC and valid at the following (left) 0000, 0300, and 0600 UTC and (right) 0900 and 1200 UTC for (a),(b) temperature, (c),(d) moisture, and (e),(f) wind. Also shown is the ensemble spread (dashed), calculated as the square root of the sum of the ensemble variance and observation error variance.

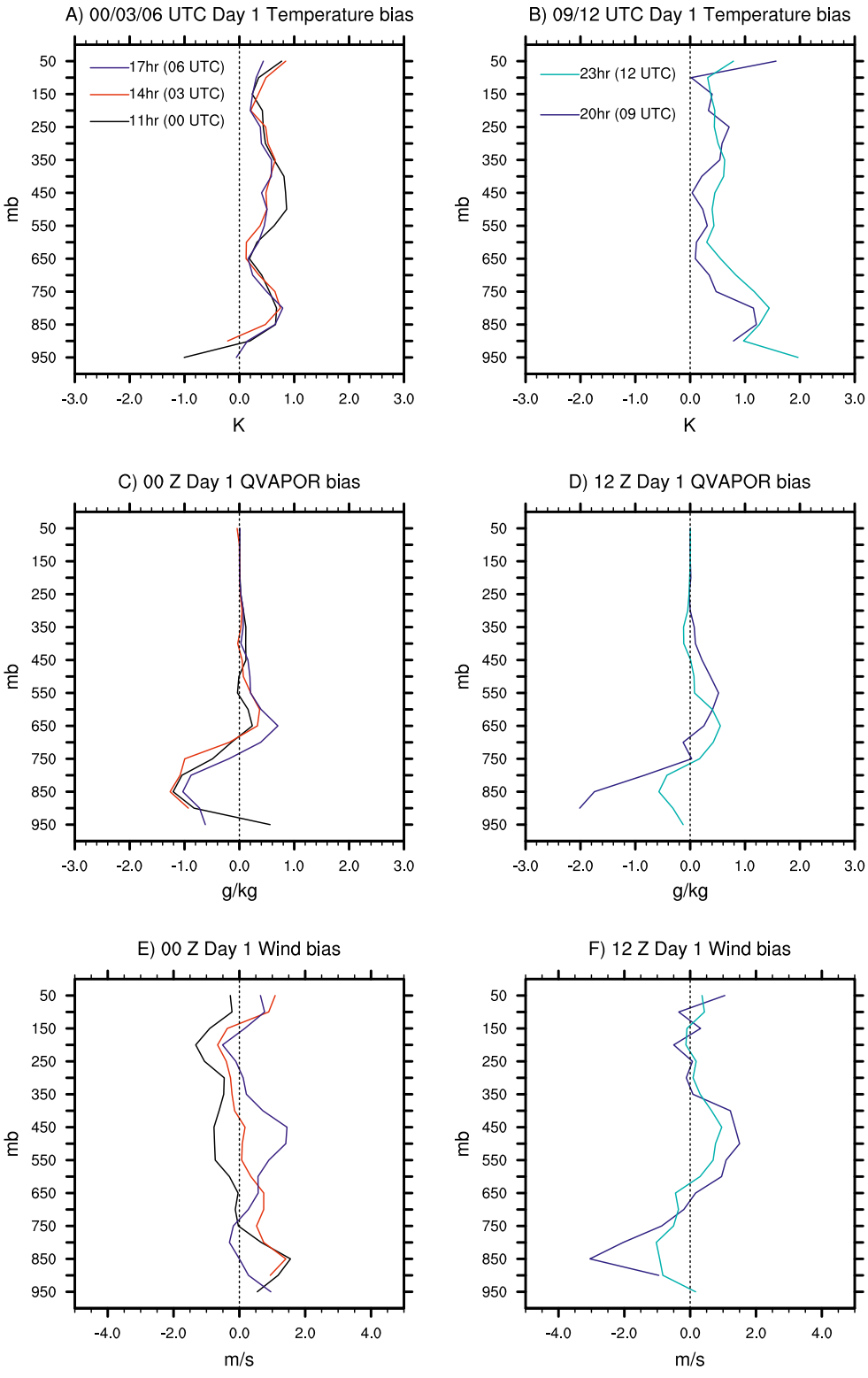

FIG. 9. As in Fig. 8, but for the bias of the ensemble mean.

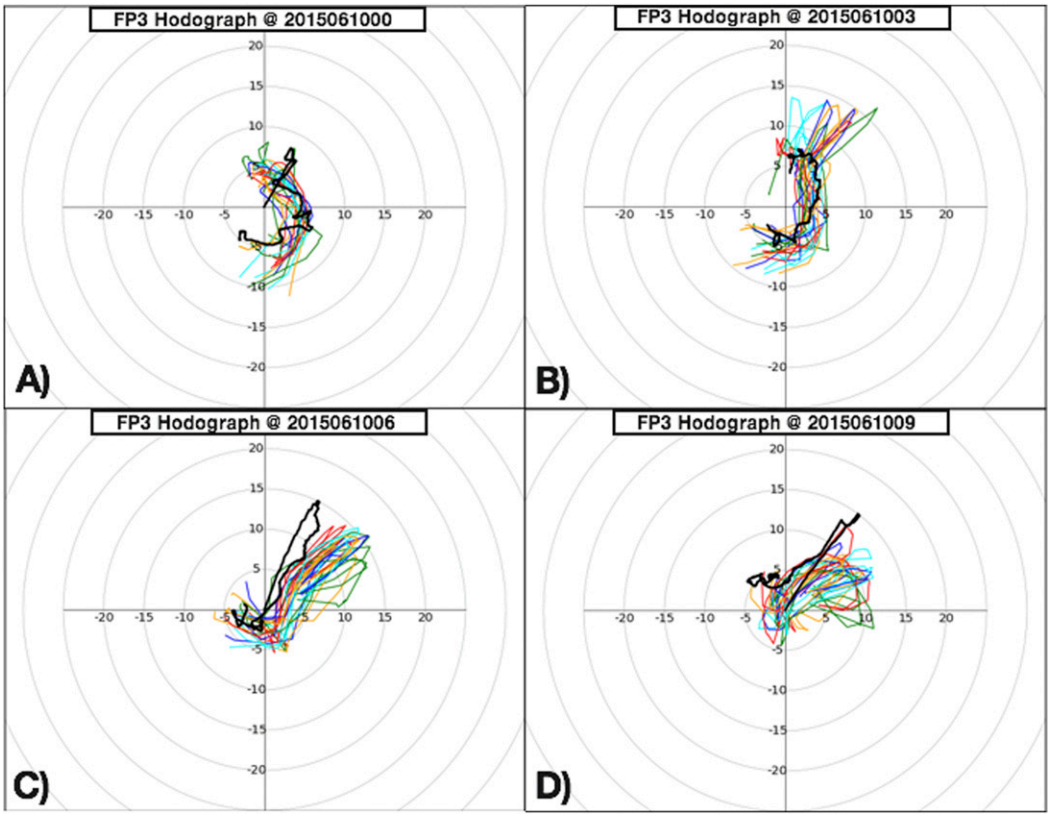

FIG. 10. Hodographs of FP3-observed sounding (black) and corresponding forecasts initialized at 1300 UTC 9 Jun 2015 and valid at (a) 0000 UTC 10 Jun, (b) 0300 UTC 10 Jun, (c) 0600 UTC 10 Jun, and (d) 0900 UTC 10 Jun 2015. Ensemble members are colored blue, green, red, cyan, or orange if they use the MYNN, QNSE, YSU, ACM2, or MYJ PBL scheme, respectively.

KDDC radar to pass over the FP3 site a little before 0700 UTC 5 June 2015 (Fig. 5a). The temperature and moisture retrievals at 10-min intervals from the FP3 AERI provide a detailed picture of the lower troposphere as the bore approaches and passes over the FP3 location (Fig. 12a; Turner 2016). After some convective clouds pass over the AERI at about forecast hours 15 and 16 (i.e., 0400 and 0500 UTC, where the red contours in Fig. 12a become temporarily cluttered), the arrival of the bore is seen at approximately 0630 UTC (Fig. 12a). Since the potential temperature and water vapor mixing ratio are conserved quantities in dry air, vertical displacement of the contours in Fig. 12a can be indicative of vertical motion. The 308-K contour is lifted ~500 m at about 0630 UTC and, then, oscillates around this new altitude, consistent with the passage of an undular bore. The evidence of an undular bore can be differentiated from a cold pool, which also typically results in lifting

TABLE 3. LLJ parameters for forecasts initialized on 9 Jun and corresponding observations.

	0300 UTC pressure at wind max (hPa)	0600 UTC pressure at wind max (hPa)	0900 UTC pressure at wind max (hPa)	0300 UTC speed at wind max ($m\,s^{-1}$)	0600 UTC speed at wind max ($m\,s^{-1}$)	0900 UTC speed at wind max ($m\,s^{-1}$)	0300 UTC direction at wind max (°)	0600 UTC direction at wind max (°)	0900 UTC direction at wind max (°)
OBS	894	910	917	7.32	15.03	15.00	194	206	217
Ensemble avg	910	904	903	10.70	13.79	10.67	199	233	243
MYNN avg	909	906	905	10.49	12.96	10.66	202	232	239
QNSE avg	907	898	905	10.91	14.71	10.05	202	242	265
YSU avg	915	908	899	9.42	13.48	10.84	189	226	233
ACM2 avg	913	905	905	11.51	14.27	11.50	193	231	243
MYJ avg	907	902	901	11.16	13.56	10.29	212	234	237

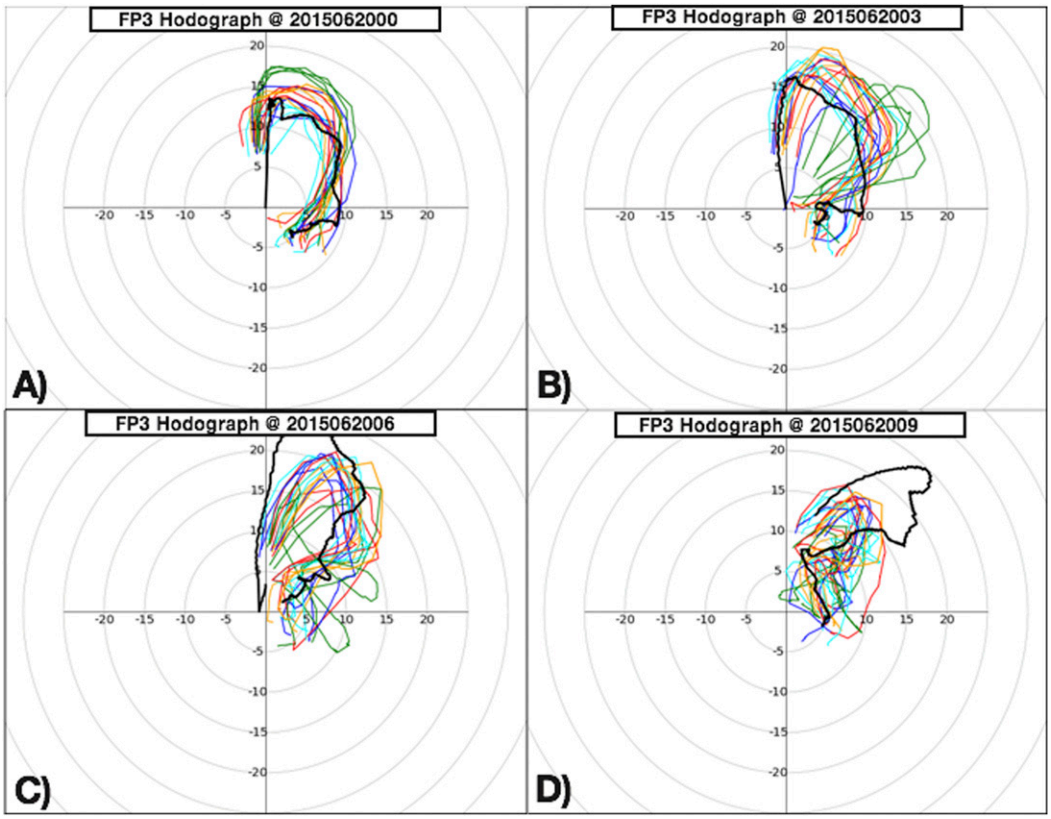

FIG. 11. As in Fig. 10, but for forecasts initialized at 1300 UTC 19 Jun and valid on 20 Jun.

and a pressure jump, by the absence of a surface temperature drop coincident with the undular bore. Since the surface cold pool does not arrive for at least another half an hour (Fig. 12a), this semipermanent lifting of an elevated layer, with superimposed oscillations, is in advance of the density current. The observations therefore support the hypothesis that the wave train observed by the KDDC radar (Fig. 5a) is an undular bore. The AERI retrievals show the bore strength (i.e., vertical displacement of the low-level stable layer) to be ~500 m. The AERI retrieval also indicates that a lifting of ~200 m of the average height of the potential temperature contours, as well as a pronounced oscillation, extends up through at least the lowest 3 km. This indicates that even though a long-lived undular bore is observed, the atmosphere is not providing a perfect duct and some of the wave energy is dispersing vertically.

The 1-km deterministic forecast also shows a borelike feature passing over the FP3 site, although the timing is earlier than observed (Fig. 5b). The 1-km forecast corresponding to the AERI observation shows the semipermanent lifting of the low-level potential temperature

TABLE 4. LLJ parameters for forecasts initialized on 19 Jun and corresponding observations. Units as in Table 3.

	0300 UTC pressure at wind max	0600 UTC pressure at wind max	0900 UTC pressure at wind max	0300 UTC speed at wind max	0600 UTC speed at wind max	0900 UTC speed at wind max	0300 UTC direction at wind max	0600 UTC direction at wind max	0900 UTC direction at wind max
OBS	888	883	896	16.34	24.44	24.75	184	196	224
Ensemble avg	881	890	898	18.62	19.75	15.27	201	207	216
MYNN avg	885	890	896	16.87	19.92	16.22	195	204	216
QNSE avg	856	900	897	19.81	17.26	12.84	223	208	222
YSU avg	882	885	897	18.29	19.67	15.82	200	208	211
ACM2 avg	894	882	899	18.73	20.98	15.58	192	208	212
MYJ avg	889	893	902	19.39	20.92	15.90	197	208	218

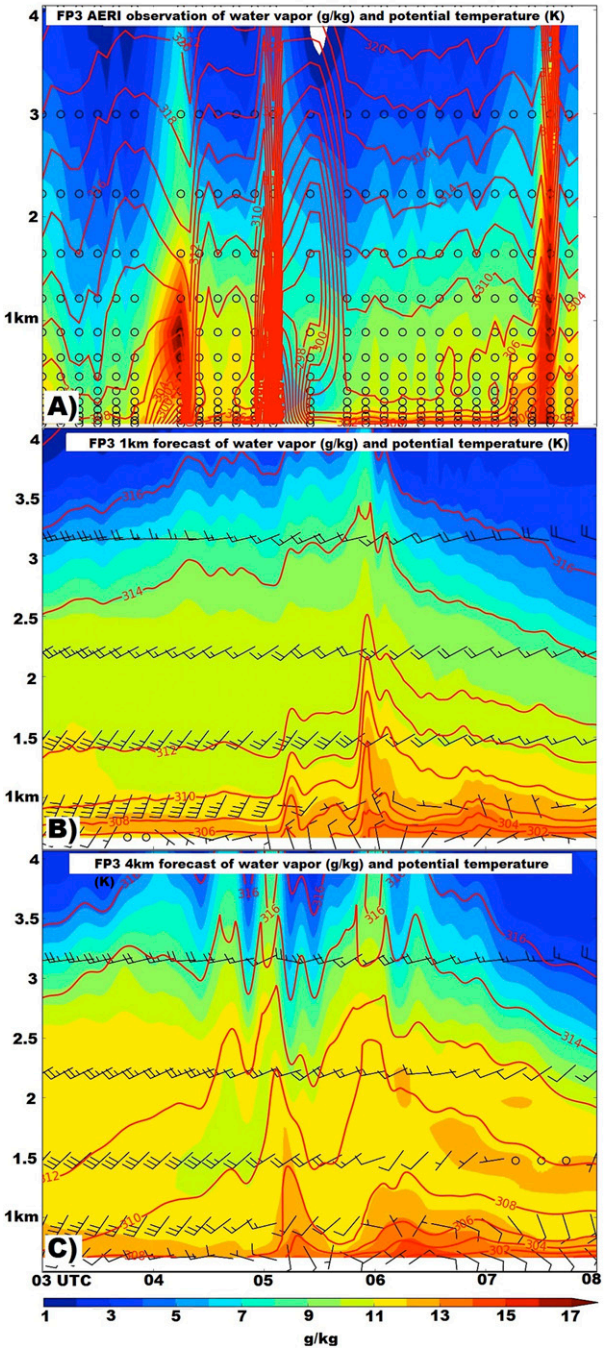

FIG. 12. (a) Time–height cross section of AERI-retrieved temperature (contour) and moisture (color fill) between 0300 and 0800 UTC 5 Jun, (b) 1-km forecast corresponding to (a) at lead times of 14–19 h (horizontal axis) for the 1300 UTC 4 Jun initialization time, and (c) corresponding forecast from the 4-km forecast driving the 1-km member (i.e., initialized from the 4-km ensemble mean analysis). Note that wind is not observed by AERI, resulting in missing wind data in (a).

and moisture contours at about 0500 UTC while the main surface cold pool arrives at about 0600 UTC (Fig. 12b). Unlike the AERI observations, the separation of the surface cold air from the borelike lifting is indistinguishable in the forecast since a 304-K contour is present at the surface just after 0500 UTC (Fig. 12b). Like the AERI observations, the impact of the borelike feature extends vertically through at least 3 km. It is also interesting to note that the influence of the bore appears to arrive about an hour earlier aloft (2500–3500 m) than at low levels (1000–2000 m; Fig. 12b). The 4-km domain that drives the 1-km forecast shows even less separation of the borelike response aloft and the surface cold pool (Fig. 12c). Also, in contrast to the steplike vertical displacement of the temperature and moisture contours in Fig. 12a and as expected for a bore, Fig. 12c shows a more gradual rising of the 310- and 312-K contours well in advance of the arrival of the cold pool. Thus, as hypothesized, the higher effective resolution [~7 times grid spacing; Skamarock (2004)] of approximately 7 km in the 1-km simulation is able to better resolve the borelike features than the 4-km grid with an effective resolution of about 28 km. Further experiments are planned to determine if 1-km grid spacing is sufficient to adequately predict the important details of bores or if even higher resolution provides further advantages. Errors in the prebore environment related to the low-level jet forecast (which affects ducting) and limited vertical resolution of low-level inversions and other features that typically appeared to be excessively smooth in the forecast soundings (not shown) in bore cases will also be addressed in these future experiments.

d. Objective evaluation of nocturnal CI prediction

Recent studies that have performed systematic and objective evaluations of CI in convection-permitting forecasts have focused on the very first storms of the day in a particular part of the domain, which typically initiate during the afternoon (Kain et al. 2013; Duda and Gallus 2013). Evaluation of nocturnal CI is even more challenging because of the even greater likelihood of nearby ongoing convection that initiated earlier in the evening or afternoon. Objectively distinguishing newly initiating convection from ongoing convection is a challenge that is addressed in the present study by defining CI as follows.

CI in this study is identified from composite reflectivity fields from the NSSL national reflectivity mosaic (Zhang et al. 2011) at hourly intervals for observed CI and from the PECAN forecasts for forecast CI. The first step in identifying CI is to convert the reflectivity fields into a binary field distinguishing active convection (composite reflectivity greater than or equal to 35 dBZ)

grid points from nonactive convection grid points. This part of the procedure is similar to a method employed in Kain et al. (2013). For each convectively active grid point, CI is considered to have occurred at that grid point if there are no grid points within a 96-km radius that were convectively active at the previous hour. This part of the procedure contrasts with the object-based method in Kain et al. (2013) since we do not attempt to identify continuity between convectively active elements at subsequent times. This simplification is motivated by the relatively coarse hourly temporal resolution of our data and was found to successfully identify new development of convection in mesobeta-scale regions that is not caused by the advection of preexisting convection.

Figure 13 shows representative examples of the performance of this method in identifying cases of observed CI. For the case in Fig. 4, this method identifies multiple-gridpoint CI "events" in three different areas at three different times, highlighted by the black boxes in Figs. 13a, 13c, and 13d. The method also sometimes identifies isolated grid points that are subjectively determined to not correspond to an independent CI event or a CI event of sufficient magnitude in terms of the coverage and duration of the initiating convection. For example, the CI grid points in southwest Nebraska in Fig. 13b are subjectively considered part of the same event as identified in Fig. 13a and therefore not verified as an independent CI event. Therefore, the objectively identified observed CI is manually quality controlled by subjectively determining which of the observed CI events correspond to a subjectively identifiable CI event, and drawing a box around the observed CI event to use for forecast evaluation. This method also works well for less pristine cases of nocturnal CI when there is convection ongoing in the same mesoalpha-scale region. For example, on 3 June 2015, CI events are identified at 0600 UTC (Fig. 13r) and 0700 UTC (Fig. 13s) that subjectively correspond to CI along the MCS cold pool and well in advance of the ongoing MCS, respectively. A few CI points are also objectively identified at 0800 UTC in east-central Colorado (Fig. 13t). However, the reflectivity appearing at 0800 UTC (Figs. 13α,β) is gone by 1000 UTC (not shown) and therefore not subjectively considered a CI event, since it did not precede a long-lasting or larger-scale convective episode. A total of 22 CI events are identified on 16 different nights, with some nights having multiple CI events as in Fig. 13. The total number of events is somewhat limited by the requirement of "pristine" CI occurring sufficiently far from other ongoing convection. The nocturnal CI forecasts are then evaluated by calculating the time difference between the observed CI time and the first CI point to appear in each ensemble member forecast within each CI event domain between the hours of 0000 and 1200 UTC and within ± 3 h of the observed CI time.

Similar to the evaluation method of Kain et al. (2013), the distributions of forecast CI times, relative to observed CI times, are shown in Fig. 14 for the full ensemble as well as single-PBL scheme subensembles. Overall, the ensemble does not show a strong bias in forecast CI time (Fig. 14a). The members with the Mellor–Yamada–Nakanishi–Niino (MYNN) PBL scheme perform the best in terms of predicting the timing of nocturnal CI (Fig. 14b). The superior performance of MYNN for nocturnal convection forecasts is consistent with the results in Part I. The QNSE members showed an early bias in the nocturnal CI predictions (Fig. 14c) while the Asymmetric Cloud Model version 2 (ACM2) and MYJ members show a late bias in the nocturnal CI predictions (Figs. 14e, f) with a pronounced bimodal distribution of the relative time of the MYJ CI forecasts (Fig. 14f). The Yonsei University (YSU) members show only a slight late bias but a lot of spread in the CI timing, as evidenced by the relatively flat histogram (Fig. 14d). While additional verification metrics would be needed for a comprehensive evaluation of all aspects of the nocturnal CI forecasts, this preliminary evaluation demonstrates a strong sensitivity of nocturnal CI forecasts to the PBL scheme. Further improvements to such predictions will therefore include a better understanding of the source of such sensitivities and the exact role of the PBL scheme in CI prediction during the nocturnal period when the boundary layer typically has a strongly stable stratification.

4. Summary and discussion

This paper describes the implementation of a real-time GSI-based multiscale ensemble DA and forecast system for the Plains Elevated Convection At Night (PECAN) field experiment. The configuration of the system is based largely on the configurations that performed best in the experiments described in Part I of this two-part study. The GSI-based EnKF was used to assimilate conventional surface and upper-air observations on an outer domain with 12-km grid spacing at 3-hourly intervals from 0000 to 1800 UTC daily. The 12-km analyses and short-term forecasts were used to drive an inner domain of the GSI-based EnKF with 4-km grid spacing over the central United States. Radar reflectivity and velocity observations were assimilated on the inner domain at 15-min intervals at 1200–1300 and 1800–1900 UTC daily. Following the main results of Part I, the ensemble used a fixed microphysics and fixed boundary layer parameterization for all members during DA, but a multiphysics configuration during the forecast period. An ensemble of 4-km forecasts was initialized

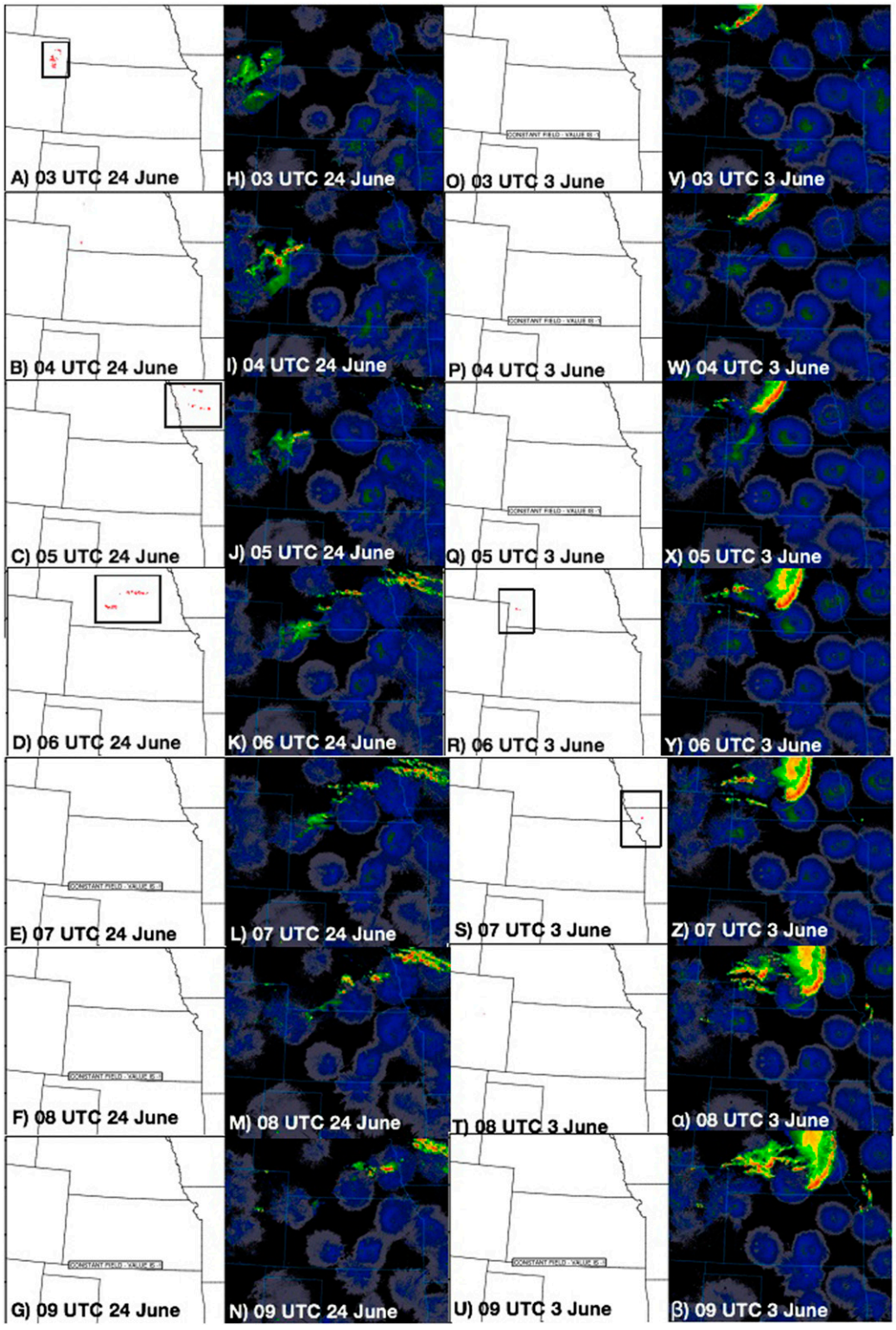

FIG. 13. Objectively identified observed CI grid points at (a)–(g) 0300–0900 UTC 24 Jun 2015 and (o)–(u) 0300–0900 UTC 3 Jun 2015. Also shown are the observed reflectivity mosaics at the corresponding times for the (h)–(n) 24 Jun and (v)–(β) 3 Jun cases. Panels overlaid with the text ''CONSTANT FIELD − VALUE IS −1'' contain no CI points.

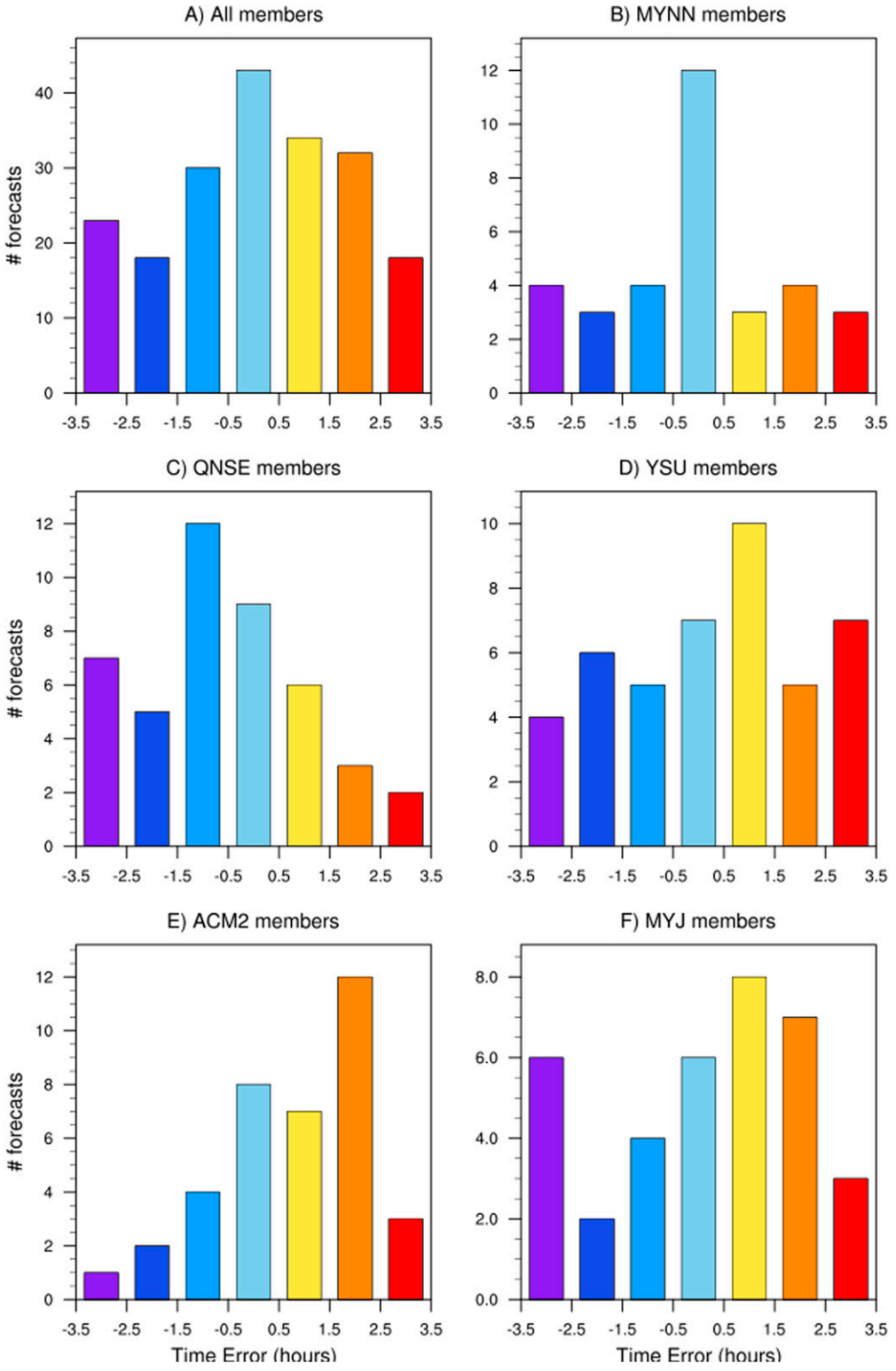

FIG. 14. Histogram of forecast CI times, relative to the observed CI time of the corresponding CI event, for (a) all ensemble members, and (b) MYNN, (c) QNSE, (d) YSU, (e) ACM2, and (f) MYJ members.

TABLE A1. Summary of forecast products provided to PECAN forecasters during the field experiment. An ex (X) indicates that the product was available for each ensemble member (column 2), the ensemble mean (column 3), the 1-km member (column 4), the ensemble probability (column 5), and the ensemble spaghetti plot (column 6) (i.e., the same contour level from all members overlaid on the same plot but in a different color). More detailed descriptions of the forecast products are provided in the text of this appendix.

Product	Members	Mean	Hi-res	Probability	Spaghetti
postage_precip		X			
postage_dbz1km		X			
postage_dbz		X			
fp	X	X			
tz_fp	X	X			
MB250	X	X			
MB500	X	X			
MB700	X	X			
MB850	X	X			
temp	X	X	X		
dewp	X	X	X		
capeXXXXm	X	X			
zlclXXXXm	X	X			
mlcape	X	X			
mucape	X	X			
uccape	X	X			
dcape	X	X			
lapse7	X	X			
lapse8	X	X			
Precip	X	X	X		
dbz_cref	X	X	X		
dbz1km	X	X	X		
MMP	X	X			
thteXXXmb	X	X			
PV335	X	X			
PV345	X	X			
isentropicXXXk	X	X			
Hgtfall	X	X			
max10m	X	X	X		
Maxuh	X	X	X		
srh_1km	X	X			
srh_3km	X	X			
srh_eff	X	X			
lljXXXXm	X	X			
convXXXXm	X	X			
conv850	X	X			
div10m			X		
Invhgt			X		
w1			X		
w5			X		
prob_dbzXX				X	
prob_precipXX				X	
prob_spdXX				X	
prob_uhXX				X	
dbz_sp(XX)					X
spd_sp(XX)					X
uh_sp(XX)					X
precip_sp(XX)					X
east1	X	X			
east1b	X	X			
east1c	X	X			
east2	X	X			
east2b	X	X			
east2c	X	X			
east3	X	X			

TABLE A1. (*Continued*)

Product	Members	Mean	Hi-res	Probability	Spaghetti
east3b	X	X			
east3c	X	X			
north1	X	X			
north1b	X	X			
north1c	X	X			
north2	X	X			
north2b	X	X			
north2c	X	X			
north3	X	X			
north3b	X	X			
north3c	X	X			

at 1300 and 1900 UTC with 20 members out to the 23-h (17 h for 1900 UTC initialization) lead time and 10 members out to the 47-h (41 h for 1900 UTC initialization) lead time. A deterministic forecast with 1-km grid spacing was also run daily from 1300 until 1200 UTC of the following day. Forecast products emphasizing the unique foci of PECAN researchers were provided to forecasters during the field experiment to help guide field operations.

The main foci of PECAN researchers are nocturnal MCSs, nocturnal CI, the nocturnal LLJs, and atmospheric bores on the nocturnal stable layer. Therefore, the forecast evaluation is conducted with particular emphasis on each of these phenomena. Quantitative precipitation forecasts are verified as a proxy for MCSs, since model-simulated precipitation and reflectivity fields played a major role in the PECAN forecasts for nocturnal MCSs. It is shown that the ensembles initialized at 1300 UTC have both greater skill and more spread in the precipitation forecasts than the ensembles initialized at 1900 UTC. A similar difference is also found between the skill of the operational NAM forecasts initialized at 1200 and 1800 UTC. Both the 1300 and 1900 UTC PECAN forecasts were more skillful than the operational NAM forecasts. A more detailed investigation of the impact of forecast initialization time on forecast skill is left for future work.

The ensemble forecasts of nonprecipitation variables are also verified against the PECAN soundings at the FP sites, with an emphasis on understanding how well the forecasts predict the development and evolution of nocturnal LLJs. The forecasts systematically show a warm and dry bias that is consistent across different lead times, as well as a high-wind bias early in the night, which transitions to a low-wind bias later in the night. Two case studies are used to further investigate the time-varying wind biases. It is shown that the model forecast LLJs tend to strengthen, veer, and weaken much faster (~3 h) than observed. These errors are sensitive to the PBL scheme for one case, with the QNSE scheme showing the most pronounced biases, but not very sensitive to the PBL scheme for another case.

The model realism of atmospheric bores on the nocturnal stable layer during PECAN is evaluated by subjectively comparing high temporal and vertical resolution temperature and moisture retrievals from AERI to the corresponding model fields as a bore passes over the AERI instrument. The observations suggest that not all of the bore energy is confined to the lowest levels, but rather extends upward through at least several kilometers. This implies that a perfect ducting layer is not necessary in order to support a long-lived undular bore. Further research should try to determine how much ducting in the actual atmosphere, as opposed to simplified two-layer models (e.g., Rottman and Simpson 1989), is needed to support bores generated by nocturnal thunderstorm outflows. Model simulations may be able to contribute to such research. Here, it is shown that the simulations with 1-km horizontal grid spacing depict the observed bores more realistically than the simulations with 4-km horizontal grid spacing. Further study is ongoing to determine the horizontal and vertical resolutions necessary to fully resolve the important features of bores.

The final aspect of nocturnal convection that is evaluated in this study is nocturnal CI. Initial subjective impressions (e.g., Fig. 4) suggested that the real-time forecast ensemble had a remarkable ability to predict certain aspects of nocturnal CI. A method of systematically and quantitatively evaluating the timing of nocturnal CI forecasts is presented, loosely following several aspects of the model CI evaluation in Kain et al. (2013). The overall ensemble predicted distributions of nocturnal CI timing that were maximized at the time of observed CI events. However, subensembles with individual PBL schemes showed quite different biases and spread of forecast CI timing for these events. Future work on improving the nocturnal CI predictability in convection-permitting models should be aware of and include attempts at understanding the source of such sensitivities. Work is also ongoing to further develop object-based verification methods specifically for CI and bore

features. These methods will be applied to the PECAN ensemble forecast dataset in future studies.

In summary, understanding and improving the model predictability of nocturnal MCSs, nocturnal CI, the nocturnal LLJs, and atmospheric bores is a key focus of the PECAN project. The real-time GSI-based ensemble data assimilation and forecast system implemented by the Multiscale data Assimilation and Predictability (MAP) team at the University of Oklahoma during the PECAN field phase, together with the unprecedented in situ and remotely sensed observations collected during PECAN, provide the data needed for an initial investigation into the current state of the art in predictability for such features. Many future studies under the broader PECAN framework will be facilitated by this work, which identifies various strengths, weaknesses, and sensitivities of the forecasts of different aspects of nocturnal convection.

Acknowledgments. The work is primarily supported by NSF Awards AGS-1359703 and AGS-1046081. This work used the Extreme Science and Engineering Discovery Environment (XSEDE), which is supported by National Science Foundation Grant ACI-1053575, and the Yellowstone machine (ark:/85065/d7wd3xhc) at NCAR's Computational and Information Systems Laboratory, sponsored by NSF. The authors thank Dave Stensrud and Dave Parsons for discussions on the overall forecast products and Kevin Haghi for discussions on calculating inversion height for the bore forecast products. The authors would also like to acknowledge the Atmospheric Radiation Measurement program for their support of the AERI instrumentation and retrieval algorithms. XW is also supported by AGS-1341878.

APPENDIX

Real-Time Forecast Products

In addition to the standard forecast products (e.g., precipitation, surface temperature, etc.) ensemble products are also tailored for the specific foci of PECAN. The forecast products are loosely grouped into the following categories, as summarized in Table A1.

a. Larger-scale and/or preconvective environment

Tz_fp*	Time–height plots at fixed Pisa locations fp1–fp6 of water vapor mixing ratio (color shading), potential temperature (contours), and wind barbs ($m\,s^{-1}$); the horizontal axis shows the forecast hour and the vertical axis the height (m)
Fp*	Forecast meteogram at each fixed Pisa location of surface temperature and dewpoint (left axis) and wind speed and total accumulated rainfall (right axis)
mb250	Constant pressure (250 mb) map of geopotential height (m) and wind (kt, where $1\,kt = 0.51\,m\,s^{-1}$)
mb500	Constant pressure (500 mb) map of geopotential height (m), wind (kt), and temperature (°C; red dashed contours)
mb700	Constant pressure (700 mb) map of geopotential height (m), wind (kt), and water vapor mixing ratio ($g\,kg^{-1}$; green contours)
mb850	Constant pressure (850 mb) map of geopotential height (m), wind (kt), and water vapor mixing ratio ($g\,kg^{-1}$; green contours)
temp	Surface (2 m) temperature (°F), 10-m wind barbs (kt), and mean sea level pressure (MSLP) contours (mb)
dewp	Surface (2 m) dewpoint temperature (°F) and 10-m wind barbs (kt)
capeXXXXm	Convective available potential energy (CAPE) of parcel lifted from XXXX m AGL and corresponding convective inhibition (CIN) contours
zlclXXXXm	Lifted condensation level (LCL; m) of parcel lifted from XXXX m AGL and corresponding level of free convection (LFC) minus LCL contours
mlcape	Mixed-layer CAPE and corresponding CIN contours
mucape	Most unstable CAPE, corresponding CIN contours, and lifted parcel level (LPL) height
uccape	Most uncapped CAPE, corresponding CIN contours, and LPL height
dcape	Downdraft CAPE
lapse7	Temperature lapse rate ($K\,km^{-1}$) between 700 and 500 mb
lapse8	Temperature lapse rate ($K\,km^{-1}$) between 700 and 500 mb

b. MCS focus

precip	Hourly accumulated precipitation (in.)
dbz_cref	Composite reflectivity
Postage_ precip	Postage stamp plots of each member's precipitation forecast; plot is located with ensemble mean products

Postage_dbz1km	Postage stamp plots of each member's 1 km AGL reflectivity forecast; plot is located with ensemble mean products
Postage_dbz	Postage stamp plots of each member's composite reflectivity forecast; plot is located with ensemble mean products
dbz1km	Reflectivity at 1 km AGL
mmp	MCS maintenance probability from Coniglio et al. (2007)
thteXXXmb	Potential temperature (K) on constant pressure (XXX mb) surfaces
pv335	Potential vorticity (PVU, where 1 PVU = 10^{-6} K kg^{-1} m^2 s^{-1}) on a 335-K surface
pv345	Potential vorticity (PVU) on a 345-K surface

c. Nocturnal CI focus

isentropicXXXk	Constant theta surface (theta = XXX K) for pressure (mb; contour), wind (barbs; kt), and moisture (g kg^{-1}; shaded)
hgtfall	Height fall; 3-h change in 500-mb height (m; only negative values plotted).

d. Severe weather/safety

max10m	Hourly maximum 10-m wind speed (kt)
maxuh	Hourly maximum updraft helicity (m^2 s^{-2})
srh_1km	Storm-relative helicity in 0–1 km AGL layer
srh_3km	Storm-relative helicity in 0–3 km AGL layer
srh_eff	Storm-relative helicity in effective inflow layer

d. Bore focus

w1	Vertical velocity (m s^{-1}) at 1 km AGL; only available for the high-resolution (hi-res) run
w5	Vertical velocity (m s^{-1}) at 5 km AGL; only available for the hi-res run
div10m	10-m wind divergence ($\times 10^4$ s^{-1}); only available for the hi-res run
invhgt	Inversion height; depth of stable layer calculated as follows, based on K. Haghi's tool: find the most stable lapse rate between two model levels in the lowest 2 km, search upward from there until the lapse rate is only conditionally unstable, stop searching at 2 km; only available for the hi-res run

e. LLJ focus

lljXXXXm	Constant height (at XXXX m AGL) plot of potential temperature (K; red contours), water vapor mixing ratio (g kg^{-1}; green contours), wind barbs (m), and wind speed (m s^{-1}; shaded)
convXXXXm	Convergence ($\times 10^5$ s^{-1}) at constant height level XXXX m AGL
conv850	Convergence ($\times 10^5$ s^{-1}) at 850 mb
east1	East–west cross section through Oklahoma City, Oklahoma (KTLX), of U wind component and divergence ($\times 10^4$ s^{-1})
east1b	East–west cross section through KTLX of V wind component and water vapor mixing ratio (g kg^{-1}; contours)
east1c	East–west cross section through KTLX of wind speed (m s^{-1}) and TKE (m^2 s^{-2})
east2	As in east1, but for east–west cross section through the Hays, Kansas, SPol
east2b	As in east1, but for east–west cross section through Hays SPol
east2c	As in east1, but for east–west cross section through Hays SPol
east3	As in east1, but for east–west cross section through Omaha, Nebraska (KOAX)
east3b	As in east1, but for east–west cross section through KOAX
east3c	As in east1, but for east–west cross section through KOAX
north1	As in east1, but for north–south cross section through Amarillo, Texas (KAMA)
north1b	As in east1, but for north–south cross section through KAMA
north1c	As in east1, but for north–south cross section through KAMA
north2	As in north1, but for north–south cross section through the Hays SPol
north2b	As in north1, but for north–south cross section through the Hays SPol
north2c	As in north1, but for north–south cross section through the Hays SPol
north3	As in north1, but for north–south cross section through KOAX
north3b	As in north1, but for north–south cross section through KOAX
north3c	As in north1, but for north–south cross section through KOAX

f. Probabilistic

prob_dbzXX	Neighborhood ensemble probability (with 48-km radius) of composite reflectivity exceeding XX dBZ
prob_precipXX	Neighborhood ensemble probability (with 48-km radius) of hourly accumulated precipitation exceeding XX hundredths of an inch
prob_spdXX	Neighborhood ensemble probability (with 48-km radius) of hourly maximum 10-m wind speed exceeding XX m s^{-1}
prob_uhXX	Neighborhood ensemble probability (with 48-km radius) of updraft helicity exceeding XX m^2 s^{-2}.

g. Spaghetti

spag_dbz_spXX	Ensemble spaghetti plot of composite reflectivity exceeding XX dBZ
spag_precip_spXX	Ensemble spaghetti plot of hourly accumulated precipitation exceeding XX hundredths of an inch
spag_spd_spXX	Ensemble spaghetti plot of hourly maximum 10-m wind speed exceeding XX m s^{-1}
spag_uh_spXX	Ensemble spaghetti plot of updraft helicity exceeding XX m^2 s^{-2}

REFERENCES

Aksoy, A., D. C. Dowell, and C. Snyder, 2010: A multicase comparative assessment of the ensemble Kalman filter for assimilation of radar observations. Part II: Short-range ensemble forecasts. *Mon. Wea. Rev.*, **138**, 1273–1292, doi:10.1175/2009MWR3086.1.

Bonner, W. D., 1966: Case study of thunderstorm activity in relation to the low-level jet. *Mon. Wea. Rev.*, **94**, 167–178, doi:10.1175/1520-0493(1966)094<0167:CSOTAI>2.3.CO;2.

Bryan, G. H., J. C. Wyngaard, and J. M. Fritsch, 2003: Resolution requirements for the simulation of deep moist convection. *Mon. Wea. Rev.*, **131**, 2394–2416, doi:10.1175/1520-0493(2003)131<2394:RRFTSO>2.0.CO;2.

Clark, R., 2016: FP3 Ellis, KS radiosonde data, version 2.0. UCAR/NCAR–Earth Observing Laboratory, accessed 1 October 2016, http://doi.org/10.5065/D6GM85DZ.

Coniglio, M. C., H. E. Brooks, S. J. Weiss, and S. F. Corfidi, 2007: Forecasting the maintenance of quasi-linear mesoscale convective systems. *Wea. Forecasting*, **22**, 556–570, doi:10.1175/WAF1006.1.

Dowell, D. C., F. Zhang, L. J. Wicker, C. Snyder, and N. A. Crook, 2004: Wind and temperature retrievals in the 17 May 1981 Arcadia, Oklahoma, supercell: Ensemble Kalman filter experiments. *Mon. Wea. Rev.*, **132**, 1982–2005, doi:10.1175/1520-0493(2004)132<1982:WATRIT>2.0.CO;2.

Du, J., and Coauthors, 2014: NCEP regional ensemble update: Current systems and planned storm-scale ensembles. *26th Conf. on Weather Analysis and Forecasting/22nd Conf. on Numerical Weather Prediction*, Atlanta, GA, Amer. Meteor. Soc., J1.4. [Available online at https://ams.confex.com/ams/94Annual/webprogram/Paper239030.html.]

Duda, J. D., and W. A. Gallus Jr., 2013: The impact of large-scale forcing on skill of simulated convective initiation and upscale evolution with convection-allowing grid spacings in the WRF. *Wea. Forecasting*, **28**, 994–1018, doi:10.1175/WAF-D-13-00005.1.

French, A. J., and M. D. Parker, 2010: The response of simulated nocturnal convective systems to a developing low-level jet. *J. Atmos. Sci.*, **67**, 3384–3408, doi:10.1175/2010JAS3329.1.

Geerts, B., and Coauthors, 2017: The 2015 Plains Elevated Convection At Night (PECAN) field project. *Bull. Amer. Meteor. Soc.*, **98**, 767–786, doi:10.1175/BAMS-D-15-00257.1.

Haase, S. P., and R. K. Smith, 1989: The numerical simulation of atmospheric gravity currents. Part II. Environments with stable layers. *Geophys. Astrophys. Fluid Dyn.*, **46**, 1–2, 35–51, doi:10.1080/03091928908208903.

Haghi, K., and D. Parson, 2014: A systematic approach to identifying and characterizing atmospheric bores and other fine-line features during IHOP_2002. *World Weather Open Science Conf.*, Montreal, QC, Canada, WMO, SCI-PS228.02. [Available online at http://wwosc2014.org/pdf/20140825-WWOSC-FinalBookofAbstracts.pdf.]

Hong, S.-Y., and J.-O. J. Lim, 2006: The WRF single-moment 6-class microphysics scheme (WSM6). *J. Korean Meteor. Soc.*, **42**, 129–151.

Janjić, Z. I., 2003: A nonhydrostatic model based on a new approach. *Meteor. Atmos. Phys.*, **82**, 271–285, doi:10.1007/s00703-001-0587-6.

Johnson, A., and X. Wang, 2017: Design and implementation of a GSI-based convection-allowing ensemble data assimilation and forecast system for the PECAN field experiment. Part I: Optimal configurations for nocturnal convection prediction. *Wea. Forecasting*, **32**, 289–315, doi:10.1175/WAF-D-16-0102.1.

——, ——, M. Xue, and F. Kong, 2011: Hierarchical cluster analysis of a convection-allowing ensemble during the Hazardous Weather Testbed 2009 Spring Experiment. Part II: Ensemble clustering over the whole experiment period. *Mon. Wea. Rev.*, **139**, 3694–3710, doi:10.1175/MWR-D-11-00016.1.

——, ——, F. Kong, and M. Xue, 2013: Object-based evaluation of the impact of horizontal grid spacing on convection-allowing forecasts. *Mon. Wea. Rev.*, **141**, 3413–3425, doi:10.1175/MWR-D-13-00027.1.

——, ——, J. R. Carley, L. J. Wicker, and C. Karstens, 2015: A comparison of multiscale GSI-based EnKF and 3DVar data assimilation using radar and conventional observations for midlatitude convective-scale precipitation forecasts. *Mon. Wea. Rev.*, **143**, 3087–3108, doi:10.1175/MWR-D-14-00345.1.

Jones, T. A., and D. J. Stensrud, 2012: Assimilating AIRS temperature and mixing ratio profiles using an ensemble Kalman filter approach for convective-scale forecasts. *Wea. Forecasting*, **27**, 541–564, doi:10.1175/WAF-D-11-00090.1.

Jung, Y., M. Xue, and M. Tong, 2012: Ensemble Kalman filter analyses of the 29–30 May 2004 Oklahoma tornadic thunderstorm using one- and two-moment bulk microphysics schemes, with verification against polarimetric radar data. *Mon. Wea. Rev.*, **140**, 1457–1475, doi:10.1175/MWR-D-11-00032.1.

Kain, J. S., and Coauthors, 2013: A feasibility study for probabilistic convection initiation forecasts based on explicit numerical guidance. *Bull. Amer. Meteor. Soc.*, **94**, 1213–1225, doi:10.1175/BAMS-D-11-00264.1.

Karyampudi, V. M., S. E. Koch, C. Chen, J. W. Rottman, and M. L. Kaplan, 1995: The influence of the Rocky Mountains on the

13–14 April 1986 severe weather outbreak. Part II: Evolution of a prefrontal bore and its role in triggering a squall line. *Mon. Wea. Rev.*, **123**, 1423–1446, doi:10.1175/1520-0493(1995)123<1423:TIOTRM>2.0.CO;2.

Lutzak, P. A., 2013: A proposal for analyzing and forecasting lower-atmospheric undular bores in the western Gulf of Mexico region. *Wea. Forecasting*, **28**, 55–76, doi:10.1175/WAF-D-12-00051.1.

Marsham, J. H., S. B. Trier, T. M. Weckwerth, and J. W. Wilson, 2011: Observations of elevated convection initiation leading to a surface-based squall line during 13 June IHOP_2012. *Mon. Wea. Rev.*, **139**, 247–271, doi:10.1175/2010MWR3422.1.

Melhauser, C., and F. Zhang, 2012: Practical and intrinsic predictability of severe convective weather at the mesoscales. *J. Atmos. Sci.*, **69**, 3350–3371, doi:10.1175/JAS-D-11-0315.1.

Parker, M., 2008: Response of simulated squall lines to low-level cooling. *J. Atmos. Sci.*, **65**, 1323–1341, doi:10.1175/2007JAS2507.1.

Parsons, D. B., B. Geerts, and T. Weckwerth, 2013: Plains Elevated Convection at Night (PECAN) scientific program overview. Dept. of Energy Rep. DOE/SC-ARM-14-035, 15 pp. [Available online at https://www.arm.gov/publications/programdocs/doe-sc-arm-14-035.pdf.]

Romine, G. S., C. S. Schwartz, J. Berner, K. R. Fossell, C. Snyder, J. L. Anderson, and M. L. Weisman, 2014: Representing forecast error in a convection-permitting ensemble system. *Mon. Wea. Rev.*, **142**, 4519–4541, doi:10.1175/MWR-D-14-00100.1.

Rottman, J. W., and J. E. Simpson, 1989: The formation of internal bores in the atmosphere: A laboratory model. *Quart. J. Roy. Meteor. Soc.*, **115**, 941–963, doi:10.1002/qj.49711548809.

Schumacher, R. S., and A. J. Clark, 2014: Evaluation of ensemble configurations for the analysis and prediction of heavy-rain-producing mesoscale convective systems. *Mon. Wea. Rev.*, **142**, 4108–4138, doi:10.1175/MWR-D-13-00357.1.

Schwartz, C. S., and Z. Liu, 2014: Convection-permitting forecasts initialized with continuously cycling limited-area 3DVAR, ensemble Kalman filter, and ''hybrid'' variational–ensemble data assimilation systems. *Mon. Wea. Rev.*, **142**, 716–738, doi:10.1175/MWR-D-13-00100.1.

——, G. S. Romine, K. R. Smith, and M. L. Weisman, 2014: Characterizing and optimizing precipitation forecasts from a convection-permitting ensemble initialized by a mesoscale ensemble Kalman filter. *Wea. Forecasting*, **29**, 1295–1318, doi:10.1175/WAF-D-13-00145.1.

——, ——, R. A. Sobash, K. R. Fossell, and M. L. Weisman, 2015a: NCAR's experimental real-time convection-allowing ensemble prediction system. *Wea. Forecasting*, **30**, 1645–1654, doi:10.1175/WAF-D-15-0103.1.

——, ——, M. L. Weisman, R. A. Sobash, K. R. Fossell, K. W. Manning, and S. B. Trier, 2015b: A real-time convection-allowing ensemble prediction system initialized by mesoscale ensemble Kalman filter analyses. *Wea. Forecasting*, **30**, 1158–1181, doi:10.1175/WAF-D-15-0013.1.

Skamarock, W. C., 2004: Evaluating mesoscale NWP models using kinetic energy spectra. *Mon. Wea. Rev.*, **132**, 3019–3032, doi:10.1175/MWR2830.1.

Snyder, C., and F. Zhang, 2003: Assimilation of simulated Doppler radar observations with an ensemble Kalman filter. *Mon. Wea. Rev.*, **131**, 1663–1677, doi:10.1175//2555.1.

Sukoriansky, S., B. Galperin, and V. Perov, 2005: Application of a new spectral theory of stably stratified turbulence to atmospheric boundary layers over sea ice. *Bound.-Layer Meteor.*, **117**, 231–257, doi:10.1007/s10546-004-6848-4.

Toth, Z., Y. Zhu, and R. Wobus, 2004: March 2004 upgrades of the NCEP global ensemble forecast system. NOAA/NCEP/EMC. [Available online at http://www.emc.ncep.noaa.gov/gmb/ens/ens_imp_news.html.]

Turner, D., 2016: FP3 AERIoe thermodynamic profile retrieval data, version 2.0. UCAR/NCAR–Earth Observing Laboratory, accessed 1 October 2016, doi:10.5065/D6Z31WV0.

——, and U. Löhnert, 2014: Information content and uncertainties in thermodynamic profiles and liquid cloud properties retrieved from the ground-based Atmospheric Emitted Radiance Interferometer (AERI). *J. Appl. Meteor. Climatol.*, **53**, 752–771, doi:10.1175/JAMC-D-13-0126.1.

UCAR/NCAR–Earth Observing Laboratory, 2016a: FP4 NCAR/EOL QC soundings, version 2.0. UCAR/NCAR–Earth Observing Laboratory, accessed 1 October 2016, doi:10.5065/D63776XH.

——, 2016b: FP5 NCAR/EOL QC soundings, version 2.0. UCAR/NCAR–Earth Observing Laboratory, accessed 1 October 2016, doi:10.5065/D6ZG6QF7.

Vanderwende, B. J., J. K. Lundquist, M. E. Rhodes, E. S. Takle, and S. L. Irvin, 2015: Observing and simulating the summertime low-level jet in central Iowa. *Mon. Wea. Rev.*, **143**, 2319–2336, doi:10.1175/MWR-D-14-00325.1.

Vermeesch, K. 2015. FP2 Greensburg, KS radiosonde data, version 1.0. UCAR/NCAR–Earth Observing Laboratory, accessed 1 October 2016, doi:10.5065/D6FQ9TPH.

Wang, Y., and X. Wang, 2017: Direct assimilation of radar reflectivity without tangent linear and adjoint of the nonlinear observation operator in the GSI-based EnVar system: Methodology and experiment with the 8 May 2003 Oklahoma City tornadic supercell. *Mon. Wea. Rev.*, **145**, 1447–1471, doi:10.1175/MWR-D-16-0231.1.

Weckwerth, T. M., and D. B. Parsons, 2006: A review of convection initiation and motivation for IHOP_2002. *Mon. Wea. Rev.*, **134**, 5–22, doi:10.1175/MWR3067.1.

——, and Coauthors, 2004: An overview of the International H_2O Project IHOP_2002) and some preliminary highlights. *Bull. Amer. Meteor. Soc.*, **85**, 253–277, doi:10.1175/BAMS-85-2-253.

Wei, M., Z. Toth, R. Wobus, and Y. Zhu, 2008: Initial perturbations based on the ensemble transform (ET) technique in the NCEP global operational forecast system. *Tellus*, **60A**, 62–79, doi:10.1111/j.1600-0870.2007.00273.x.

Wheatley, D. M., N. Yussouf, and D. J. Stensrud, 2014: Ensemble Kalman filter analyses and forecasts of a severe mesoscale convective system using different choices of microphysics schemes. *Mon. Wea. Rev.*, **142**, 3243–3263, doi:10.1175/MWR-D-13-00260.1.

——, K. H. Knopfmeier, T. A. Jones, and G. J. Creager, 2015: Storm-scale data assimilation and ensemble forecasting with the NSSL Experimental Warn-on-forecast System. Part I: Radar data experiments. *Wea. Forecasting*, **30**, 1795–1817, doi:10.1175/WAF-D-15-0043.1.

Wilson, J. W., and R. D. Roberts, 2006: Summary of convective storm initiation and evolution during IHOP: Observational and modeling perspective. *Mon. Wea. Rev.*, **134**, 23–47, doi:10.1175/MWR3069.1.

Yussouf, N., and D. J. Stensrud, 2010: Impact of phased-array radar observations over a short assimilation period: Observing system simulation experiments using an ensemble Kalman filter. *Mon. Wea. Rev.*, **138**, 517–538, doi:10.1175/2009MWR2925.1.

Zhang, F., C. Snyder, and J. Sun, 2004: Impacts of initial estimate and observation availability on convective-scale data assimilation with an ensemble Kalman filter. *Mon. Wea. Rev.*, **132**, 1238–1253, doi:10.1175/1520-0493(2004)132<1238:IOIEAO>2.0.CO;2.

Zhang, J., and Coauthors, 2011: National Mosaic and Multi-Sensor QPE (NMQ) system: Description, results, and future plans. *Bull. Amer. Meteor. Soc.*, **92**, 1321–1338, doi:10.1175/2011BAMS-D-11-00047.1.